Table 1 Affected putative splicing *cis*-elements in *COL1A1* exon 45 predicted by ESEfinder, ESRsearch and PESXs

Sequence variation	Normal allele	Variant allele	Predicted effect	Score[d]		Putative *trans*-factor
				Normal	Variant	
rs1800215	CC**G**CCGG	CC**A**CCGG[a]	Gain	1.622	4.231	SRp40
rs1800217	CTGT**T**GGC	CTGT**C**GGC[c]	Gain		n.a.	
c.3226G>A	CGCC**G**G	CGCC**A**G[b]	Gain		n.a.	
	CC**G**GTCCT	CC**A**GTCCT[c]	Gain		n.a.	
c.3226G>A+rs1800215	CC**G**CC**G**G	CC**A**CC**A**G[a]	Gain	1.622	3.663	SRp40
c.3226G>T	CGCC**G**G	CGCC**T**G[b]	Gain		n.a.	
c.3226G>T+rs1800215	CC**G**CC**G**G	CC**A**CC**T**G[a]	Loss	3.498	0.571	SF2/ASF
c.3235G>A	CTGTC**G**G	CTGTC**A**G[a]	Loss	2.492	0.713	SF2/ASF
	CTGTC**G**GC	CTGTC**A**GC[c]	Loss		n.a.	
	TGTC**G**GC	TGTC**A**GC[a]	Gain	1.058	3.613	SRp40
	GTC**G**GC	GTC**A**GC[b]	Gain		n.a.	
	C**G**GCCCTG	C**A**GCCCTG[c]	Gain		n.a.	
c.3244G>T	**G**GCGCCCG	**T**GCGCCCG[a]	Loss	3.109	1.059	SC35
	GGCGCC	**T**GCGCC[a]	Gain	0.721	3.531	SRp55
c.3244G>T+rs1800217	TGT**TG**GC	TGT**CT**GC[a]	Gain	−1.326	3.367	SRp40
c.3253G>A	CGT**G**GC	CGT**A**GC[a]	Loss	2.940	2.331	SRp55

Variant nucleotides are shown in bold and underlined

n.a. not applicable

[a] ESEfinder

[b] ESRsearch

[c] PESXs

[d] Default threshold values employed by ESEfinder are SRp40 = 2.67, SF2/ASF = 1.867, SC35 = 2.383 and SRp55 = 2.676

12.5% regions of the entire genome. We first sought for a mutation responsible for hyperuricemia in 24 genes (see Table 3 and Suppl. Table 2) that are involved in urate metabolisms and excretion, but found none in either patient. We then scrutinized SNPs in ten genes that are known to be associated with hyperuricemia and identified 12 SNPs (Table 3). In this analysis, we excluded SNPs with a minor allelic frequency of 0.01 or less. Among the 12 SNPs, rs2231142 in *ABCG2* as well as rs3825016 and rs11231825 in *SLC22A12* are previously reported and will be addressed in the discussion. We traced the three SNPs in F1, F2 and F3 by capillary sequencing and found that variable dosages of these SNPs were observed in hyperuricemic as well as in normouricemic individuals (Fig. 1).

A missense mutation in *GPATCH8* is likely to lead to hyperuricemia in the Japanese family (F1)

After eliminating SNPs in the dbSNP132 database, only three non-synonymous variants remained shared between II-2 and II-3 on chr 17; c.602A>G in exon 2 of *KRBA2* at 17p13.1, c.206C>T in exon 3 of *ZPBP2* (MIM# 608499) at 17q12 (Fig. 3a) and c.2935G>C in exon 8 of *GPATCH8* at 17q21.31 (Fig. 3b). Capillary sequencing revealed that variants in *ZPBP2* and *GPATCH8* cosegregated with hyperuricemia in F1, but the *KRBA2* variant did not. These two variants were not detected in F2, F3, F4, 100 normal human individuals or exomes of 50 Tibetans (Yi et al. 2010). In addition, exome-capture resequencing of VIII-2 detected no mutations in *ZPBP2* and *GPATCH8*.

ZPBP2 c.206C>T and *GPATCH8* c.2935G>C predict amino acid substitutions of p.T69I and p.A979P, respectively. Threonine 69 and the flanking amino acids of *ZPBP2* are not conserved across mammalian species. Additionally, an SNP rs35591738 mutates the N-terminal proline at codon 68, and an SNP rs34272593 causes a frameshift at codon 70 (Fig. 3a). In contrast, alanine 979 and the flanking amino acids of *GPATCH8* are in the serine-rich region and are highly conserved across mammalian species (Fig. 3b). PolyPhen-2 (Adzhubei et al. 2010) predicted that *ZPBP2* p.T69I was benign with a score of 0.025 and *GPATCH8* p.A979P was damaging with a score of 0.988, where 1.0 was the worst score. Similarly, SIFT (Kumar et al. 2009) predicted that *ZPBP2* p.T69I was tolerated with a score of 0.38 and *GPATCH8* p.A979P was damaging with a score of 0.00, where a score < 0.05 was predicted to be deleterious.

Table 2 Splice site strength of *COL1A1* exon 45 predicted by the NetGene2 and the Splice Site Prediction by Neural Network

Sequence variation	NetGene2		Splice Site Prediction by Neural Network	
	Confidence		Score	
	Acceptor	Donor	Acceptor	Donor
Wild type	0.97	0.93	0.98	0.95
rs1800215	–	–	–	–
rs1800217	–	–	–	–
c.3226G>A	–	0.89	–	–
c.3226G>A+rs1800215	0.94	0.89	–	–
c.3226G>A+rs1800217	–	0.89	–	–
c.3226G>T	0.94	0.87	–	–
c.3226G>T+rs1800215	0.94	0.86	–	–
c.3226G>T+rs1800217	0.94	0.87	–	–
c.3235G>A	0.94	0.87	–	–
c.3235G>A+rs1800215	0.94	0.86	–	–
c.3235G>A+rs1800217	0.94	0.87	–	–
c.3244G>T	0.94	0.86	–	–
c.3244G>T+rs1800215	0.94	0.86	–	–
c.3244G>T+rs1800217	0.94	0.86	–	–
c.3253G>A	0.94	0.88	0.52[a]	–
c.3253G>A+rs1800215	0.94	0.87	0.52[a]	–
c.3253G>A+rs1800217	–	0.89	–	–

– symbol represents being identical to the wild-type

[a] In addition to the native splice acceptor site of 0.98, a cryptic splice acceptor site 'AG' is generated at c.3253_3254

Table 3 Twelve SNPs identified by exome resequensing in five out of ten genes associated with hyperuricemia

Ch	Gene	Position	Nuc.	Amino acid	AF	dbSNP	II-2	II-3	VIII-2
1	*AGL*	100,336,361	C > T	Syn.	0.7	rs2230306	T/T	–/T	–/T
4	*ABCG2*[b]	89,034,551	G > A	Syn.	0.02	rs35622453	–/–	–/–	–/A
		89,052,323	C > A	Q141K	0.31	rs2231142	–/A	A/A	–/–
		89,061,114	G > A	V12M	0.19	rs2231137	–/A	–/–	–/A
4	*SLC2A9*[b]	9,909,923	C > T	P350L	0.33	rs2280205	–/T	–/T	–/–
		9,922,130	G > A	R294H	0.72	rs3733591	–/A	–/–	–/A
		9,998,440	G > A	Syn.	0.54	rs10939650	–/A	A/A	–/A
		10,022,981	G > A	G25R	0.43	rs2276961	–/A	–/A	–/–
		10,027,542	G > A	A17T	0.06	rs6820230	–/–	–/A	–/A
11	*SLC22A12*[b]	64,359,286	C > T	Syn.	0.21	rs3825016	–/T	T/T	–/T
		64,360,274	C > T	Syn.	0.81	rs11231825	–/T	–/–	–/T
12	*PFKM*		n.d.						
16	*UMOD*[b]		n.d.						
17	*G6PC*		n.d.						
X	*HPRT1*[a]		n.d.						
X	*PRPS1*[a]		n.d.						
X	*MAOA*	43,591,036	G > T	Syn.	0.3	rs6323	–/–	T/T	T/T

[a] The gene is associated with purine metabolism

[b] The gene is associated with renal excretion of urate

– symbol represents in the patients' genotypes mean being identical to the reference nucleotides

Syn synonymous nucleotide change, *AF* allelic frequency of the changed nucleotide, *n.d.* no SNPs are detected

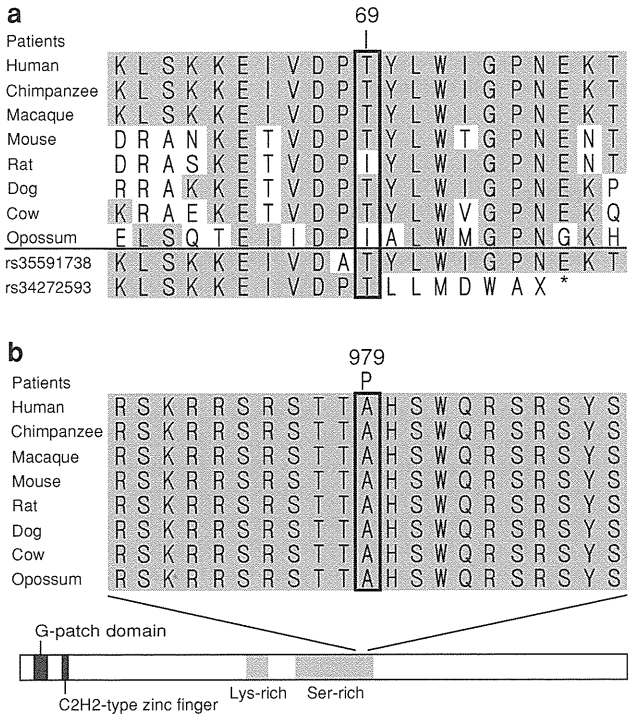

Fig. 3 Conservation of 21 amino acid segments encoded by *ZPBP2* and *GPATCH8* in mammals. Locations of non-synonymous variants identified in the Japanese family (F1) are *boxed*. Amino acids identical to human are *shaded*. **a** c.206C>T predicts p.T69I in *ZPBP2*. T69 is not conserved in rat and opossum. An SNP rs35591738 predicts p.P68A, and an SNP rs34272593 induces a frameshift. **b** c.2935G>C predicts p.A979P in *GPATCH8*. The mutation is located at the C-terminal end of the serine-rich region

Discussion

Phenotypic variabilities of OI mutations

We identified a heteroallelic c.3235G>A mutation in *COL1A1* exon 45 in a Japanese family with mild OI type I. The c.3235G>A mutation has been previously reported in six families with OI types I (Hartikka et al. 2004; Mottes et al. 1992; Roschger et al. 2008) and IV (Marini et al. 2007). *COL1A1* exon 45 encodes six of the 338 Gly-X–Y triplet repeats. Four additional mutations have been reported in exon 45 (Constantinou et al. 1989; Lund et al. 1997; Marini et al. 2007), and all substitute Ser or Cys for Gly (Fig. 2a) with mild to lethal phenotypes. Among the five mutations, two mutations introducing Cys result in a lethal type II, whereas three mutations introducing Ser give rise to milder types I, III and IV. This notion, however, cannot be applied to the other exons according to the human type I collagen mutation database (http://www.le.ac.uk/genetics/collagen/).

Being prompted by a report that more than 16–20% of exonic mutations disrupt an ESE (Gorlov et al. 2003), we asked if a mutation disrupting an ESE in exon 45 causes skipping of an inframe exon 45 and exhibits a severe dominant negative phenotype. Three Web-based programs predict that all the five mutations and the two SNPs affect 16 putative exonic splicing *cis*-elements (Table 1). We thus constructed and analyzed 18 minigenes carrying all possible combinations of the five mutations and two SNPs (Fig. 2b), but found that none affected pre-mRNA splicing (Fig. 2c). Our analysis suggests that the currently available algorithms of splicing *trans*-factors cannot efficiently predict splicing *cis*-elements. This is likely because the recognition motifs of splicing *trans*-factors are mostly determined by in vitro SELEX experiments. A recently developed technique, the high throughput sequencing coupled to crosslinking immunoprecipitation method (HITS-CLIP), enables us to extensively determine RNA segments recognized by a specific splicing *trans*-factor in vivo (Licatalosi et al. 2008; Yeo et al. 2009). Accumulation of knowledge with the HITS-CLIP technology will enable us to construct dependable algorithms to efficiently predict splicing *cis*-elements.

In addition to the phenotypic variability among similar mutations in the same exon, the same mutation often exhibits variable phenotypes, although the variability is usually less (Lund et al. 1996). This is also true for our families. In the Japanese family (F1), two sons (II-1 and II-3) experienced many fractures, whereas the father (I-1) and another son (II-2) had no history of fractures. In the Italian family (F2), the son suffered from many fractures, but his affected mother did not (Mottes et al. 1992). In the Canadian family (F3), the father was classified as OI type IV, whereas his daughter as OI type I (Roschger et al. 2008). Variable clinical phenotypes of the c.3235G>A mutation is likely due to differences in environmental factors or to SNPs in disease-modifying genes, but the molecular bases have not been elucidated in any type of OI.

Molecular basis of hyperuricemia

In F1, hyperuricemia cosegregated with OI type 1. Although no known genes causing hyperuricemia are on chr 17 where *COL1A1* is located, two candidate genes of *PRPSAP1* and *PRPSAP2* are on chr 17. Capillary sequencing of these genes, however, detected no mutation. We thus employed exome-capture resequencing analysis of two siblings in F1 to search for a responsible gene for hyperuricemia. We first looked into SNPs in the 10 candidate genes that are associated with hyperuricemia, purine metabolism and renal excretion, and found 12 SNPs in 10 genes (Table 3). Among them, three SNPs in *ABCG2* (rs2231142) and *SLC22A12* (rs3825016 and rs11231825) are previously reported markers for hyperuricemia and/or gout.

Dehghan et al. (2008) report that rs2231142 in *ABCG2* is associated with gout by a genome-wide association study (OR = 1.74 and 1.71 in white and black participants, respectively). Woodward et al. (2009) showed a significant association between rs2231142 and hyperuricemia (OR = 1.68) in a population-based study of 14,783 individuals. Kolz et al. (2009) demonstrated that rs2231142 elevated the serum urate concentration more strongly in men than in women by meta-analysis of 28,141 individuals. Stark et al. (2009) analyzed 683 patients with gout and indicated a significant association between rs2231142 and gout (OR = 1.37). Although rs2231142 is an attractive causative SNP, our normouricemic subjects were also heterozygous for rs2231142.

Graessler et al. (2006) analyzed 389 German individuals with primary hyperuricemia and found that rs3825016 and rs11231825 in *SLC22A12* were significantly associated with reduced fractional excretion of urate in the kidney. Tabara et al. (2010) analyzed 1,526 normal Japanese individuals retrospectively and longitudinally, and clarified that rs11231825 was associated with reduced urate excretion and with future development of hyperuricemia. Again, although the two SNPs are attractive causes of hyperuricemia, we observe variable dosages of these SNPs even in our normouricemic subjects.

We next looked into neighboring genes of *COL1A1* without considering the functions of the gene products, and identified that two missense variants in *ZPBP2* and *GPATCH8* cosegregated with the *COL1A1* mutation in F1. Neither variant was detected in 300 normal alleles or in dbSNP132. *ZPBP2* p.T69I, however, is unlikely to be pathogenic for three reasons: lack of conservation in mammals; two missense/frameshifting SNPs at or close to the variant site (Fig. 3a); and the benign predicted outcome by PolyPhen-2 and SIFT. On the other hand, p.A979P in *GPATCH8* substitutes an amino acid in the highly conserved serine-rich region (Fig. 3b), and the substitution is predicted to damage the structure and function of the protein by in silico analysis. *GPATCH8* encodes the G patch domain-containing protein 8 that harbors both an RNA-processing domain and a zinc finger domain. *GPATCH8* is expressed in a wide variety of human tissues including skeletal muscles, brain, heart, pancreas, liver and kidney (McKinney et al. 2004). Functions of the *GPATCH8* gene product, however, have not been studied to date. The p.A979P variant in *GPATCH8* is highly likely to be associated with hyperuricemia in F1, but it may also cause another yet unidentified phenotype that cosegregates with OI.

Acknowledgments We would like to thank the families for their participation in this study. We are grateful to Dr. Kunio Ihara at the Center for Gene Research of Nagoya University for the SOLiD sequencing analysis and Keiko Itano for technical assistance. This work was supported by Grants-in-Aid from the Ministry of Education, Culture, Sports, Science and Technology of Japan, and the Ministry of Health, Labor and Welfare of Japan.

References

Adzhubei IA, Schmidt S, Peshkin L, Ramensky VE, Gerasimova A, Bork P, Kondrashov AS, Sunyaev SR (2010) A method and server for predicting damaging missense mutations. Nat Methods 7:248–249

Alanay Y, Avaygan H, Camacho N, Utine GE, Boduroglu K, Aktas D, Alikasifoglu M, Tuncbilek E, Orhan D, Bakar FT, Zabel B, Superti-Furga A, Bruckner-Tuderman L, Curry CJ, Pyott S, Byers PH, Eyre DR, Baldridge D, Lee B, Merrill AE, Davis EC, Cohn DH, Akarsu N, Krakow D (2010) Mutations in the gene encoding the RER protein FKBP65 cause autosomal-recessive osteogenesis imperfecta. Am J Hum Genet 87:572–573

Allen GE, Rogers FB, Lansbury J (1955) Osteogenesis imperfecta tarda with hyperuricemia and gout: report of three cases. Am J Med Sci 230:30–32

Baldridge D, Schwarze U, Morello R, Lennington J, Bertin TK, Pace JM, Pepin MG, Weis M, Eyre DR, Walsh J, Lambert D, Green A, Robinson H, Michelson M, Houge G, Lindman C, Martin J, Ward J, Lemyre E, Mitchell JJ, Krakow D, Rimoin DL, Cohn DH, Byers PH, Lee B (2008) CRTAP and LEPRE1 mutations in recessive osteogenesis imperfecta. Hum Mutat 29:1435–1442

Bodian DL, Madhan B, Brodsky B, Klein TE (2008) Predicting the clinical lethality of osteogenesis imperfecta from collagen glycine mutations. Biochemistry 47:5424–5432

Brunak S, Engelbrecht J, Knudsen S (1991) Prediction of human mRNA donor and acceptor sites from the DNA sequence. J Mol Biol 220:49–65

Cabral WA, Chang W, Barnes AM, Weis M, Scott MA, Leikin S, Makareeva E, Kuznetsova NV, Rosenbaum KN, Tifft CJ, Bulas DI, Kozma C, Smith PA, Eyre DR, Marini JC (2007) Prolyl 3-hydroxylase 1 deficiency causes a recessive metabolic bone disorder resembling lethal/severe osteogenesis imperfecta. Nat Genet 39:359–365

Cartegni L, Chew SL, Krainer AR (2002) Listening to silence and understanding nonsense: exonic mutations that affect splicing. Nat Rev Genet 3:285–298

Cartegni L, Wang J, Zhu Z, Zhang MQ, Krainer AR (2003) ESEfinder: a web resource to identify exonic splicing enhancers. Nucleic Acids Res 31:3568–3571

Christiansen HE, Schwarze U, Pyott SM, AlSwaid A, Al Balwi M, Alrasheed S, Pepin MG, Weis MA, Eyre DR, Byers PH (2010) Homozygosity for a missense mutation in SERPINH1, which encodes the collagen chaperone protein HSP47, results in severe recessive osteogenesis imperfecta. Am J Hum Genet 86:389–398

Constantinou CD, Nielsen KB, Prockop DJ (1989) A lethal variant of osteogenesis imperfecta has a single base mutation that substitutes cysteine for glycine 904 of the alpha 1(I) chain of type I procollagen. The asymptomatic mother has an unidentified mutation producing an overmodified and unstable type I procollagen. J Clin Invest 83:574–584

Dalgleish R (1997) The human type I collagen mutation database. Nucleic Acids Res 25:181–187

Dehghan A, Kottgen A, Yang Q, Hwang SJ, Kao WL, Rivadeneira F, Boerwinkle E, Levy D, Hofman A, Astor BC, Benjamin EJ, van Duijn CM, Witteman JC, Coresh J, Fox CS (2008) Association of three genetic loci with uric acid concentration and risk of gout: a genome-wide association study. Lancet 372:1953–1961

Doring A, Gieger C, Mehta D, Gohlke H, Prokisch H, Coassin S, Fischer G, Henke K, Klopp N, Kronenberg F, Paulweber B, Pfeufer A, Rosskopf D, Volzke H, Illig T, Meitinger T, Wichmann HE, Meisinger C (2008) SLC2A9 influences uric acid concentrations with pronounced sex-specific effects. Nat Genet 40:430–436

Fairbrother WG, Yeh RF, Sharp PA, Burge CB (2002) Predictive identification of exonic splicing enhancers in human genes. Science 297:1007–1013

Gibbs RA, Caskey CT (1987) Identification and localization of mutations at the Lesch–Nyhan locus by ribonuclease A cleavage. Science 236:303–305

Glorieux FH, Rauch F, Plotkin H, Ward L, Travers R, Roughley P, Lalic L, Glorieux DF, Fassier F, Bishop NJ (2000) Type V osteogenesis imperfecta: a new form of brittle bone disease. J Bone Miner Res 15:1650–1658

Glorieux FH, Ward LM, Rauch F, Lalic L, Roughley PJ, Travers R (2002) Osteogenesis imperfecta type VI: a form of brittle bone disease with a mineralization defect. J Bone Miner Res 17:30–38

Goren A, Ram O, Amit M, Keren H, Lev-Maor G, Vig I, Pupko T, Ast G (2006) Comparative analysis identifies exonic splicing regulatory sequences—the complex definition of enhancers and silencers. Mol Cell 22:769–781

Gorlov IP, Gorlova OY, Frazier ML, Amos CI (2003) Missense mutations in hMLH1 and hMSH2 are associated with exonic splicing enhancers. Am J Hum Genet 73:1157–1161

Graessler J, Graessler A, Unger S, Kopprasch S, Tausche AK, Kuhlisch E, Schroeder HE (2006) Association of the human urate transporter 1 with reduced renal uric acid excretion and hyperuricemia in a German Caucasian population. Arthritis Rheum 54:292–300

Hart TC, Gorry MC, Hart PS, Woodard AS, Shihabi Z, Sandhu J, Shirts B, Xu L, Zhu H, Barmada MM, Bleyer AJ (2002) Mutations of the UMOD gene are responsible for medullary cystic kidney disease 2 and familial juvenile hyperuricaemic nephropathy. J Med Genet 39:882–892

Hartikka H, Kuurila K, Korkko J, Kaitila I, Grenman R, Pynnonen S, Hyland JC, Ala-Kokko L (2004) Lack of correlation between the type of COL1A1 or COL1A2 mutation and hearing loss in osteogenesis imperfecta patients. Hum Mutat 24:147–154

Hebsgaard SM, Korning PG, Tolstrup N, Engelbrecht J, Rouze P, Brunak S (1996) Splice site prediction in *Arabidopsis thaliana* pre-mRNA by combining local and global sequence information. Nucleic Acids Res 24:3439–3452

Ishizuka T, Ahmad I, Kita K, Sonoda T, Ishijima S, Sawa K, Suzuki N, Tatibana M (1996) The human phosphoribosylpyrophosphate synthetase-associated protein 39 gene (PRPSAP1) is located in the chromosome region 17q24–q25. Genomics 33:332–334

Katashima R, Iwahana H, Fujimura M, Yamaoka T, Itakura M (1998) Assignment of the human phosphoribosylpyrophosphate synthetase-associated protein 41 gene (PRPSAP2) to 17p11.2–p12. Genomics 54:180–181

Kolz M, Johnson T, Sanna S, Teumer A, Vitart V, Perola M, Mangino M, Albrecht E, Wallace C, Farrall M, Johansson A, Nyholt DR, Aulchenko Y, Beckmann JS, Bergmann S, Bochud M, Brown M, Campbell H, Connell J, Dominiczak A, Homuth G, Lamina C, McCarthy MI, Meitinger T, Mooser V, Munroe P, Nauck M, Peden J, Prokisch H, Salo P, Salomaa V, Samani NJ, Schlessinger D, Uda M, Volker U, Waeber G, Waterworth D, Wang-Sattler R, Wright AF, Adamski J, Whitfield JB, Gyllensten U, Wilson JF, Rudan I, Pramstaller P, Watkins H, Doering A, Wichmann HE, Spector TD, Peltonen L, Volzke H, Nagaraja R, Vollenweider P, Caulfield M, Illig T, Gieger C (2009) Meta-analysis of 28,141 individuals identifies common variants within five new loci that influence uric acid concentrations. PLoS Genet 5:e1000504

Kumar P, Henikoff S, Ng PC (2009) Predicting the effects of coding non-synonymous variants on protein function using the SIFT algorithm. Nat Protoc 4:1073–1081

Lalonde E, Albrecht S, Ha KC, Jacob K, Bolduc N, Polychronakos C, Dechelotte P, Majewski J, Jabado N (2010) Unexpected allelic heterogeneity and spectrum of mutations in Fowler syndrome revealed by next-generation exome sequencing. Hum Mutat 31:918–923

Langmead B, Trapnell C, Pop M, Salzberg SL (2009) Ultrafast and memory-efficient alignment of short DNA sequences to the human genome. Genome Biol 10:R25

Lapunzina P, Aglan M, Temtamy S, Caparros-Martin JA, Valencia M, Leton R, Martinez-Glez V, Elhossini R, Amr K, Vilaboa N, Ruiz-Perez VL (2010) Identification of a frameshift mutation in Osterix in a patient with recessive osteogenesis imperfecta. Am J Hum Genet 87:110–114

Licatalosi DD, Mele A, Fak JJ, Ule J, Kayikci M, Chi SW, Clark TA, Schweitzer AC, Blume JE, Wang X, Darnell JC, Darnell RB (2008) HITS-CLIP yields genome-wide insights into brain alternative RNA processing. Nature 456:464–469

Lund AM, Schwartz M, Skovby F (1996) Variable clinical expression in a family with OI type IV due to deletion of three base pairs in COL1A1. Clin Genet 50:304–309

Lund AM, Skovby F, Schwartz M (1997) Serine for glycine substitutions in the C-terminal third of the alpha 1(I) chain of collagen I in five patients with nonlethal osteogenesis imperfecta. Hum Mutat 9:378–382

Marini JC, Forlino A, Cabral WA, Barnes AM, San Antonio JD, Milgrom S, Hyland JC, Korkko J, Prockop DJ, De Paepe A, Coucke P, Symoens S, Glorieux FH, Roughley PJ, Lund AM, Kuurila-Svahn K, Hartikka H, Cohn DH, Krakow D, Mottes M, Schwarze U, Chen D, Yang K, Kuslich C, Troendle J, Dalgleish R, Byers PH (2007) Consortium for osteogenesis imperfecta mutations in the helical domain of type I collagen: regions rich in lethal mutations align with collagen binding sites for integrins and proteoglycans. Hum Mutat 28:209–221

McKinney JL, Murdoch DJ, Wang J, Robinson J, Biltcliffe C, Khan HM, Walker PM, Savage J, Skerjanc I, Hegele RA (2004) Venn analysis as part of a bioinformatic approach to prioritize expressed sequence tags from cardiac libraries. Clin Biochem 37:953–960

Morello R, Bertin TK, Chen Y, Hicks J, Tonachini L, Monticone M, Castagnola P, Rauch F, Glorieux FH, Vranka J, Bachinger HP, Pace JM, Schwarze U, Byers PH, Weis M, Fernandes RJ, Eyre DR, Yao Z, Boyce BF, Lee B (2006) CRTAP is required for prolyl 3-hydroxylation and mutations cause recessive osteogenesis imperfecta. Cell 127:291–304

Mottes M, Sangalli A, Valli M, Gomez Lira M, Tenni R, Buttitta P, Pignatti PF, Cetta G (1992) Mild dominant osteogenesis imperfecta with intrafamilial variability: the cause is a serine for glycine alpha 1(I) 901 substitution in a type-I collagen gene. Hum Genet 89:480–484

Ng SB, Turner EH, Robertson PD, Flygare SD, Bigham AW, Lee C, Shaffer T, Wong M, Bhattacharjee A, Eichler EE, Bamshad M, Nickerson DA, Shendure J (2009) Targeted capture and massively parallel sequencing of 12 human exomes. Nature 461:272–276

Ng SB, Bigham AW, Buckingham KJ, Hannibal MC, McMillin MJ, Gildersleeve HI, Beck AE, Tabor HK, Cooper GM, Mefford HC, Lee C, Turner EH, Smith JD, Rieder MJ, Yoshiura K, Matsumoto N, Ohta T, Niikawa N, Nickerson DA, Bamshad MJ, Shendure J (2010a) Exome sequencing identifies MLL2 mutations as a cause of Kabuki syndrome. Nat Genet 42:790–793

Ng SB, Buckingham KJ, Lee C, Bigham AW, Tabor HK, Dent KM, Huff CD, Shannon PT, Jabs EW, Nickerson DA, Shendure J,

Bamshad MJ (2010b) Exome sequencing identifies the cause of a Mendelian disorder. Nat Genet 42:30–35

Ohno K, Milone M, Shen X-M, Engel AG (2003) A frameshifting mutation in *CHRNE* unmasks skipping of the preceding exon. Hum Mol Genet 12:3055–3066

Rauch F, Glorieux FH (2004) Osteogenesis imperfecta. Lancet 363:1377–1385

Reese MG, Eeckman FH, Kulp D, Haussler D (1997) Improved splice site detection in Genie. J Comput Biol 4:311–323

Roessler BJ, Nosal JM, Smith PR, Heidler SA, Palella TD, Switzer RL, Becker MA (1993) Human X-linked phosphoribosylpyrophosphate synthetase superactivity is associated with distinct point mutations in the PRPS1 gene. J Biol Chem 268:26476–26481

Roschger P, Fratzl-Zelman N, Misof BM, Glorieux FH, Klaushofer K, Rauch F (2008) Evidence that abnormal high bone mineralization in growing children with osteogenesis imperfecta is not associated with specific collagen mutations. Calcif Tissue Int 82:263–270

Sillence DO, Senn A, Danks DM (1979) Genetic heterogeneity in osteogenesis imperfecta. J Med Genet 16:101–116

Stark K, Reinhard W, Grassl M, Erdmann J, Schunkert H, Illig T, Hengstenberg C (2009) Common polymorphisms influencing serum uric acid levels contribute to susceptibility to gout, but not to coronary artery disease. PLoS One 4:e7729

Tabara Y, Kohara K, Kawamoto R, Hiura Y, Nishimura K, Morisaki T, Kokubo Y, Okamura T, Tomoike H, Iwai N, Miki T (2010) Association of four genetic loci with uric acid levels and reduced renal function: the J-SHIPP Suita study. Am J Nephrol 32:279–286

van Dijk FS, Nesbitt IM, Zwikstra EH, Nikkels PG, Piersma SR, Fratantoni SA, Jimenez CR, Huizer M, Morsman AC, Cobben JM, van Roij MH, Elting MW, Verbeke JI, Wijnaendts LC, Shaw NJ, Hogler W, McKeown C, Sistermans EA, Dalton A, Meijers-Heijboer H, Pals G (2009) PPIB mutations cause severe osteogenesis imperfecta. Am J Hum Genet 85:521–527

Vitart V, Rudan I, Hayward C, Gray NK, Floyd J, Palmer CN, Knott SA, Kolcic I, Polasek O, Graessler J, Wilson JF, Marinaki A, Riches PL, Shu X, Janicijevic B, Smolej-Narancic N, Gorgoni B, Morgan J, Campbell S, Biloglav Z, Barac-Lauc L, Pericic M, Klaric IM, Zgaga L, Skaric-Juric T, Wild SH, Richardson WA, Hohenstein P, Kimber CH, Tenesa A, Donnelly LA, Fairbanks LD, Aringer M, McKeigue PM, Ralston SH, Morris AD, Rudan P, Hastie ND, Campbell H, Wright AF (2008) SLC2A9 is a newly identified urate transporter influencing serum urate concentration, urate excretion and gout. Nat Genet 40:437–442

Wang Z, Rolish ME, Yeo G, Tung V, Mawson M, Burge CB (2004) Systematic identification and analysis of exonic splicing silencers. Cell 119:831–845

Ward LM, Rauch F, Travers R, Chabot G, Azouz EM, Lalic L, Roughley PJ, Glorieux FH (2002) Osteogenesis imperfecta type VII: an autosomal recessive form of brittle bone disease. Bone 31:12–18

Woodward OM, Kottgen A, Coresh J, Boerwinkle E, Guggino WB, Kottgen M (2009) Identification of a urate transporter, ABCG2, with a common functional polymorphism causing gout. Proc Natl Acad Sci USA 106:10338–10342

Yeo GW, Coufal NG, Liang TY, Peng GE, Fu XD, Gage FH (2009) An RNA code for the FOX2 splicing regulator revealed by mapping RNA–protein interactions in stem cells. Nat Struct Mol Biol 16:130–137

Yi X, Liang Y, Huerta-Sanchez E, Jin X, Cuo ZX, Pool JE, Xu X, Jiang H, Vinckenbosch N, Korneliussen TS, Zheng H, Liu T, He W, Li K, Luo R, Nie X, Wu H, Zhao M, Cao H, Zou J, Shan Y, Li S, Yang Q, Asan Ni P, Tian G, Xu J, Liu X, Jiang T, Wu R, Zhou G, Tang M, Qin J, Wang T, Feng S, Li G, Huasang Luosang J, Wang W, Chen F, Wang Y, Zheng X, Li Z, Bianba Z, Yang G, Wang X, Tang S, Gao G, Chen Y, Luo Z, Gusang L, Cao Z, Zhang Q, Ouyang W, Ren X, Liang H, Zheng H, Huang Y, Li J, Bolund L, Kristiansen K, Li Y, Zhang Y, Zhang X, Li R, Li S, Yang H, Nielsen R, Wang J, Wang J (2010) Sequencing of 50 human exomes reveals adaptation to high altitude. Science 329:75–78

Zhang XH, Chasin LA (2004) Computational definition of sequence motifs governing constitutive exon splicing. Genes Dev 18:1241–1250

Zhang XH, Kangsamaksin T, Chao MS, Banerjee JK, Chasin LA (2005) Exon inclusion is dependent on predictable exonic splicing enhancers. Mol Cell Biol 25:7323–7332

Pediatr Radiol
DOI 10.1007/s00247-011-2132-1

ORIGINAL ARTICLE

Radiological evaluation of dysmorphic thorax of paternal uniparental disomy 14

Osamu Miyazaki · Gen Nishimura · Masayo Kagami · Tsutomu Ogata

Received: 21 November 2010 / Revised: 31 January 2011 / Accepted: 1 February 2011

Abstract
Background The "coat-hanger" sign of the ribs with a bell-shaped thorax has been known as a radiological hallmark of the paternal uniparental disomy 14 (upd(14)pat).
Objective To quantitatively determine the differences in thoracic deformity between upd(14)pat and other bone diseases with thoracic hypoplasia and to establish the age-dependent evolution.
Materials and methods The subjects comprised 11 children with upd(14)pat. The angle between the 6th posterior rib and the horizontal axis was measured (coat hanger angle; CHA). The ratio of the mid- to widest thorax diameter (M/W ratio) was calculated for the bell-shaped thorax.
Results CHA ranged from +28.5 to 45° (mean; 35.1°±5.2) in upd(14)pat, and from −19.8 to 21° (−3.3±13°) in bone dysplasias ($p<0.01$). The M/W ratio ranged from 58% to 93% (75.4±10) in upd(14)pat, and from 80% to 92% (86.8±3.3) in bone dysplasias ($p<0.05$). Serial radiographs revealed that CHA remained constant during early childhood, while the M/W ratio gradually increased with age.
Conclusion The "coat-hanger" sign of upd(14)pat provides a distinctive radiological gestalt that makes it possible to differentiate the disorder from other skeletal dysplasias. By contrast, the bell-shaped thorax is significant only in the neonatal period.

Keywords UPD14 · Plain radiograph · Coat-hanger sign · Bell-shaped thorax

O. Miyazaki (✉)
Department of Radiology,
National Center for Child Health and Development,
2-10-1 Okura,
Seatagaya-ku, Tokyo 157-8535, Japan
e-mail: osamu-m@rc4.so-net.ne.jp

G. Nishimura
Department of Radiology,
Tokyo Metropolitan Children's Medical Center,
2-8-29 Musashidai,
Fuchu-shi, Tokyo 183-8561, Japan

M. Kagami · T. Ogata
Division of Clinical Genetics and Molecular Medicine,
National Center for Child Health and Development,
2-10-1 Okura,
Seatagaya-ku, Tokyo 157-8535, Japan

Introduction

Uniparental disomy (UPD) refers to the inheritance of a pair of chromosomes from only one parent. UPD is a relatively common phenomenon. The inheritance of both, or parts of both, maternal chromosomes (heterodisomic maternal UPD) has been found to become more prevalent as parental age becomes more advanced [1]. It is well established that UPD for chromosomes 6, 7, 11, 14 and 15 is associated with recognized syndromes, including Prader-Willi syndrome (maternal UPD 15), Angelman syndrome (paternal UPD 15), and Beckwith-Wiedemann syndrome (paternal UPD 11) [2].

The paternal UPD 14 phenotype (upd(14)pat) is a recently recognized genetic condition that is caused by an aberration of the imprinting center in chromosome 14. The clinical hallmarks of upd(14)pat are thoracic hypoplasia and abdominal wall defect. Mild facial dysmorphism and developmental delay are also noted. In addition, upd(14)pat presents with a distinctive radiological finding: the "coat-hanger" appearance of the ribs and a bell-shaped thorax [3]. In the past, upd(14)pat was often misdiagnosed as bone dysplasias with thoracic hypoplasia, as in Jeune syndrome [4], because attention was not paid to the morphological differences of the thorax between upd(14)pat and other genetic bone diseases. Previous reports on

Published online: 24 May 2011

upd(14)pat have been based on a single case or a limited number of cases. To date, there has been no radiological report involving a large series of upd(14)pat cases. Although a previous report suggested that the dysmorphic thorax in upd(14)pat ameliorated in the mid-childhood period [5], it remains to be determined how the thoracic deformity in upd (14)pat evolves with age. The purpose of this study was to quantitatively determine the differences in the thoracic deformity between upd(14)pat and other genetic bone diseases, and to establish the age-dependent radiological evolution of the thoracic hypoplasia in upd(14)pat.

Materials and methods

The subjects comprised 11 children (6 girls and 5 boys) with upd(14)pat phenotypes proven on molecular grounds [5, 6]. Three of the 11 children had been managed in our hospital, and 8 were referred to our institution for molecular diagnosis. The molecular diagnoses included seven cases of paternal uniparental disomy, two of microdeletion and two of epimutation. The initial radiographs available for the analysis were obtained in the neonatal period (n=8), and at 7, 24 and 32 months of age (n=1). Sequential radiological evaluation was feasible in 4 of 11 children up to 5 years of age. The study was approved by the institutional review board at the National Center for Child Health and Development.

To assess for the "coat-hanger" sign, the angle between the 6th posterior rib and the horizontal axis was measured (coat hanger angle, CHA; an upward angle was defined as +, and a downward angle as −). The ratio of the mid- to widest thorax diameter (M/W ratio) was calculated for the bell-shaped thorax (Figs. 1, 2). For comparison, both indexes were evaluated in nine cases with bone dysplasia with thoracic hypoplasia, including thanatophoric dysplasia (n=6), Ellis-van Creveld syndrome (n=2) and asphyxiating thoracic dysplasia (n=1). These cases were selected from our radiology database. The children's ages ranged from 21 weeks of gestation to 6 years of age (mean: 11 months of age). Both indexes were also evaluated in five children with respiratory distress syndrome (RDS) and without skeletal abnormalities that could be assessed to determine the evolution of the normal thoracic morphology. In the RDS group, serial follow-up radiographs were available from the neonatal period up to 2 years to 6 years of age (mean 4.2). The measurement of CHA and M/W ratio was performed using an accessory digital tool from a PACS

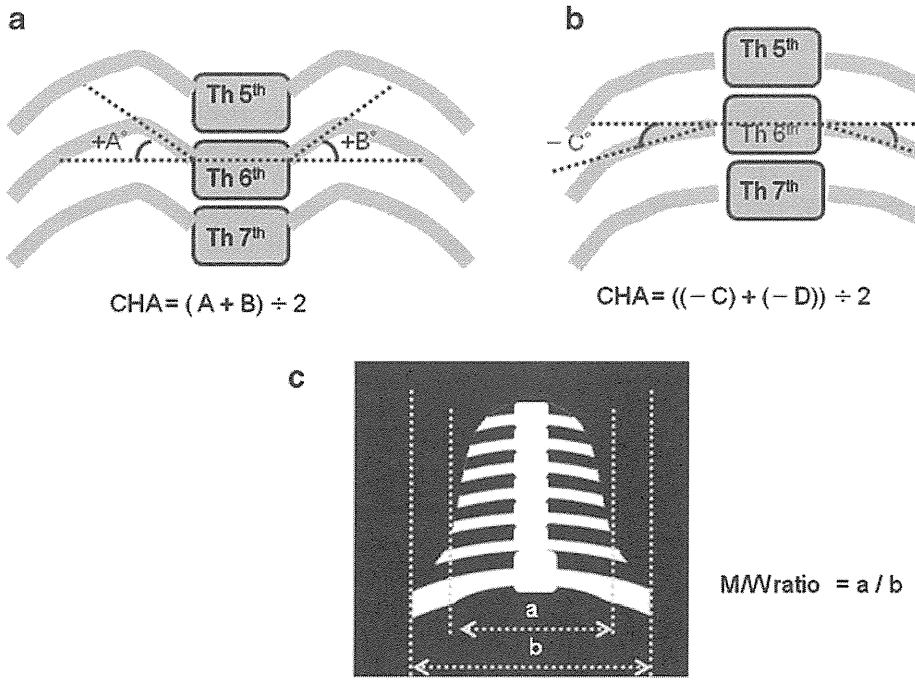

Fig. 1 **a**, **b** Diagram of coat-hanger angle (CHA) and mid/widest ratio. CHA refers to the average of the angles between the peak point of both 6th posterior ribs and the horizontal axis. If there is no peak point of the 6th posterior ribs, the center of the ribs is utilized instead. The horizontal axis is defined as a line passing through two points of both 6th cost-vertebral junctions. An upward angle is defined as +, and a downward angle as −. CHA is thought to be a quantitative index of the coat-hanger sign. **c** The ratio of mid- to widest thorax (M/W ratio) refers to the ratio of the narrowest diameter of the mid-thorax to the widest diameter of the basal thorax. In most cases with upd(14)pat, the thorax showed medial concavity with the top of approximately the 6th rib (the narrowest mid-thorax) and downward sloping toward the 9th to 11th ribs (the widest basal thorax). M/W ratio is thought to be a quantitative index of dysmorphic bell-shaped thorax

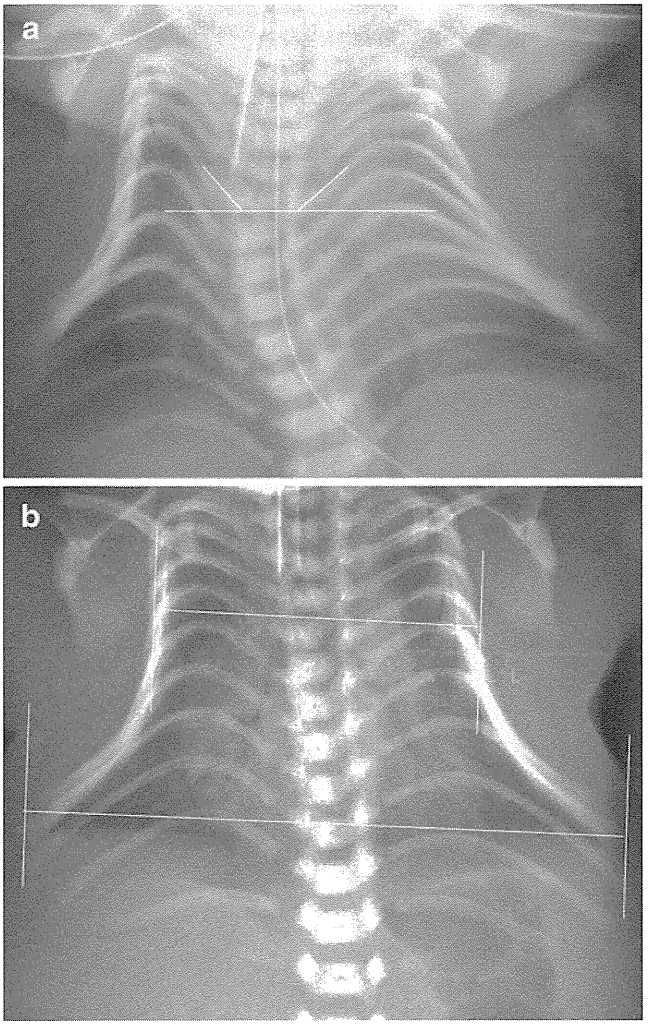

Fig. 2 Examples of CHA and M/W ratio. **a** The 6th posterior ribs show upward bowing that provides the coat-hanger sign. The CHA of this case (patient #7 in Table 1) was 45° (the measurement was 48° for the right and 42° for the left). **b** The M/W ratio was 58% in this case (patient #5 in Table 1). This is an example of severe bell-shaped thorax in upd(14)pat

system (Centricity ™ RA 1000 Ver.3.0, GE Healthcare, Milwaukee, WI) on the PACS monitor, or using area and protractor commercial software (Lenara Ver2.21, Vector, Tokyo) on a personal computer monitor. An unpaired two-tailed t-test was used for statistical evaluation.

Results

Clinical and measurement data are summarized in Table 1 and Fig. 3. All 11 children with upd(14)pat showed a severe upward sweep of the posterior rib or increased CHA, ranging from +28.5 to 45° (mean ± SD; 35.1°±5.2) (Figs. 2, 3). Children with bone dysplasias presented with variable manifestations of the posterior rib, and CHA ranged from −19.8 to 21° (mean ± SD; −3.3±13°) (Figs. 3, 4). The difference in CHA was statistically significant between the upd(14)pat and bone dysplasia groups ($P<0.01$). According to this result, approximately +25° was the estimated cut-off line of CHA to differentiate upd(14)pat from skeletal dysplasias (Fig. 3). The M/W ratio ranged from 58% to 93% (mean±SD; 75.4±10) in the upd(14)pat group, while it ranged between 80% and 92% (mean±SD; 86.8±3.3) in the skeletal dysplasia group (Fig. 3). The difference an unpaired two-tailed t-test in the M/W ratio was, though statistically significant, less conspicuous than that in CHA ($P<0.05$). There was considerable overlap in the range of the M/W ratio between the upd(14)pat and skeletal dysplasia groups.

The age-dependent evolution of CHA and M/W ratio in the upd(14)pat and RDS groups is shown in Fig. 5. In the four children with upd(14)pat, CHA remained unaltered regardless of age, ranging from 25° to 45°. In the RDS group ($n=5$), CHA was constant regardless of age, ranging from −6.4 to 10° (mean −0.6) at birth and from −8 to 7.3° thereafter (Fig. 5). The M/W ratio of the upd(14)pat group was smaller than that of the RDS group in the neonatal period. However, it increased gradually with age and finally caught up with that observed in the RDS group (Figs. 6, 7).

Discussion

The clinical manifestations of upd(14)pat have been well established to date. The hallmarks of this condition include a small thorax, laryngomalacia, hypoplastic abdominal wall, short limbs with joint contractures, craniofacial dysmorphism, and mental retardation [2]. In addition, several reports on the prenatal diagnosis of upd(14)pat suggested the common occurrence of polyhydramnios and preterm delivery in upd(14)pat [2, 7]. A few reports on upd (14)pat have detailed the radiological manifestations, such as disproportionately short limbs, spurring of lower femoral and upper tibial metaphyses, absent glenoid fossa, shortened iliac wing with flaring, thin and elongated clavicle, hypoplastic scapular neck, kyphoscoliosis, hypoplasia of the maxilla and mandible, a broad nasal bridge, wide sutures and multiple wormian skull bones, contractures of the wrists with ulnar deviation, and stippled calcification [3, 8–10]. However, these findings are so mild that alone they do not determine the diagnosis. Instead, the distinctive thoracic deformity in upd(14)pat, termed the coat-hanger sign as introduced by Offiah et al. [3], enables a definitive diagnosis to be made. Sutton et al. [8] described the thoracic deformity of upd(14)pat as "anterior ribs bowed caudally (downward), and posterior portions of the ribs bowed cranially (upward)," and these configurations are combined in the characteristic coat-hanger sign of the ribs

Table 1 Summary of clinical details, measurement of rib angle, coat-hanger angle (CHA), and ratio of mid- to widest thorax (M/W ratio). *GW* gestational week, *TD* thanatophoric dysplasia, *ATD* asphyxiating thoracic dysplasia, *EvC* Ellis-van Creveld syndrome, *RDS* respiratory distress syndrome

Case	Gender	Age (months)[a]	Molecular or clinical diagnosis	Right rib angle (°)	Left rib angle (°)	CHA (°)	M/W ratio (%)
upd(14)pat patients							
1	f	0	upd	36	31	33.5	80
2	m	0	upd	43	41	42	66
3	m	0	upd	27	46	36.5	80
4	m	7	upd	32	38	35	80
5	m	0	deletion	27	30	28.5	58
6	f	0	Epimutation	35	23	29	77
7	f	0	Epimutation	48	42	45	65
8	f (45,XX)	0	upd	30	34	32	69
9	f	0	upd	46	32	39	74
10	m	24	upd	28	38	33	87
11	f	32	decision	32	33	32.5	93
mean		5.7		35	35.82	35.1	75.4
TD group patients							
1	m	21GW	TD	−9.9	−13.7	−11.8	80
2	f	6	TD	−3.7	12	1	85.6
3	m	21GW	TD	−11.7	−13.9	−12.8	86
4	Unknown	20GW	TD	−19.6	−20	−19.8	86
5	m	0	TD	7	−12	−2.5	87
6	m	21GW	TD	−15	−21	−18	87
7	m	84	ATD	4	2	3	88
8	f	11	EvC	9.6	10.3	9.95	90
9	m	24	EvC	14	28	21	92
mean		11		−2.8	−3.1	−3.3	86.8
RDS patients							
1	m	0	RDS	1.8	4	2.9	90
2	m	0	RDS	1.2	−14	−6.4	81.7
3	m	0	RDS	−6.9	−4.1	−5.2	84
4	m	0	RDS	−6	−2	−4	91
5	f	0	RDS	11.3	8.7	10	85
mean		0		0.28	−1.48	−0.54	86.3

[a] Age at which time the initial radiograph was available

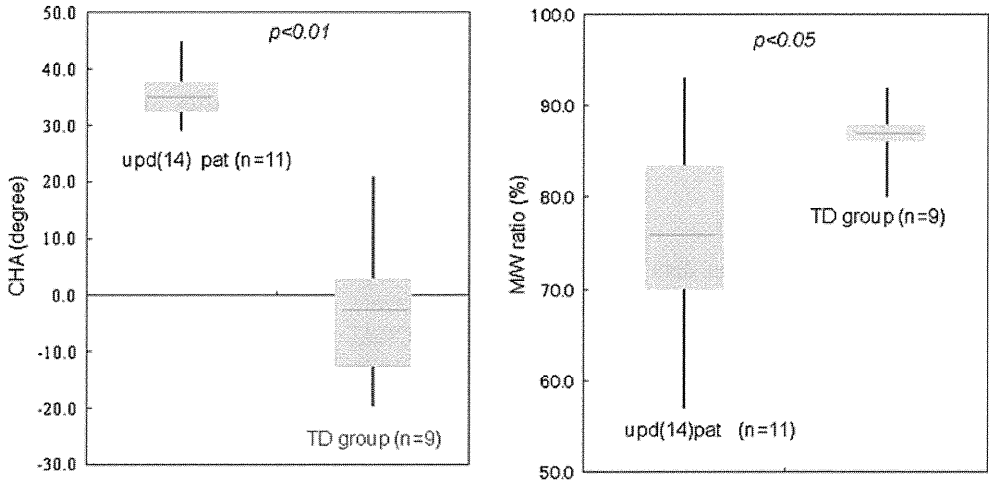

Fig. 3 Box plot of CHA and M/W ratio with the median, interquartile interval and range

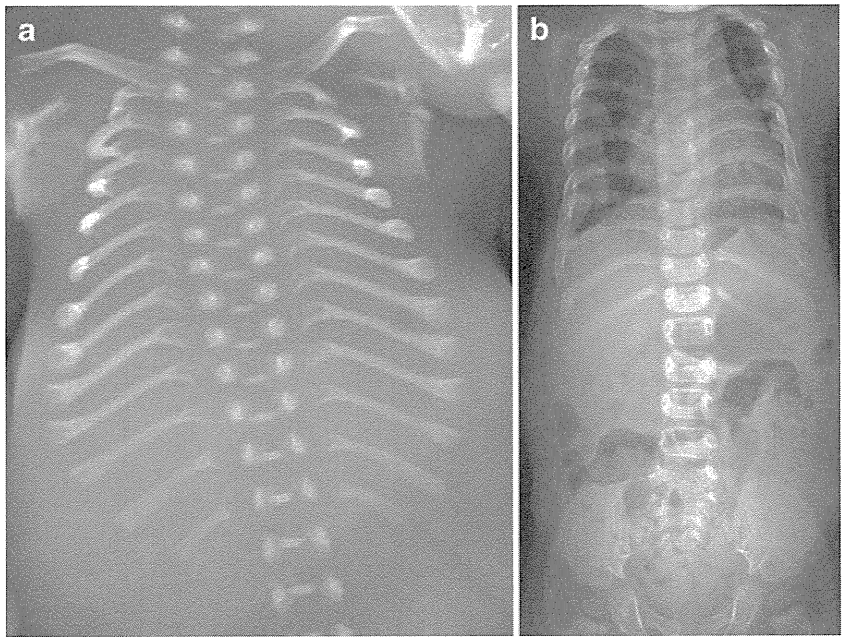

Fig. 4 Examples of the thoracic appearance and measurement of bone dysplasias with thoracic hypoplasia. **a** Thanatophoric dysplasia (TD) type 1 (stillbirth at 21 weeks of gestation). Note a narrow thorax with cupped anterior ends as well as short long bones with metaphyseal cupping. The posterior ribs show downward sloping. The CHA was −18°, and the M/W ratio was 87%. Despite the presence of severe thoracic hypoplasia in TD, its morphology is different from that seen in upd(14)pat (Fig. 2). **b** Ellis-van Creveld (EvC) syndrome (2 years of age). The thorax appears narrow, and a trident appearance of the acetabula is seen. Posterior ribs show upward sloping. The CHA was 21°, and the M/W ratio was 92%. The morphological pattern of the thorax differs from that of upd(14)pat

on the chest radiograph. Sutton et al. concluded that the skeletal phenotype in upd(14)pat involves primarily the axial skeleton, with little to no effect on the long bones. Very small changes of the long bones in upd(14)pat correspond with those of the mouse model (UPD of the distal segment of mouse chromosome 12) [11]. Consequently, it is assumed that imprinted genes on human chromosome 14 and mouse chromosome 12 play a role in axial skeletal formation and ossification [8, 11].

In the subsequent articles on upd(14)pat, all 11 affected children presented unexceptionally with the coat-hanger sign [5, 6, 12]. It was thought that the upward posterior rib bowing and downward anterior rib bowing (the coat-hanger appearance) in upd(14)pat contrast with the horizontally oriented ribs generally seen in disorders with thoracic hypoplasia. Based on the radiological sign, along with other radiological findings, it is not difficult to differentiate upd(14)pat from other genetic disorders involv-

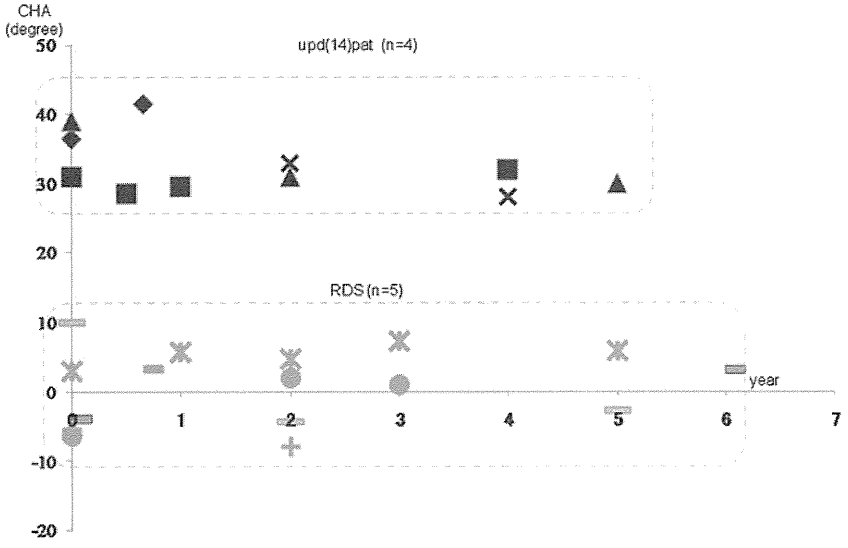

Fig. 5 Comparative observation of age-dependent transition of CHA between the upd(14)pat and respiratory distress syndrome (RDS) groups. Individual shapes represent individual patients

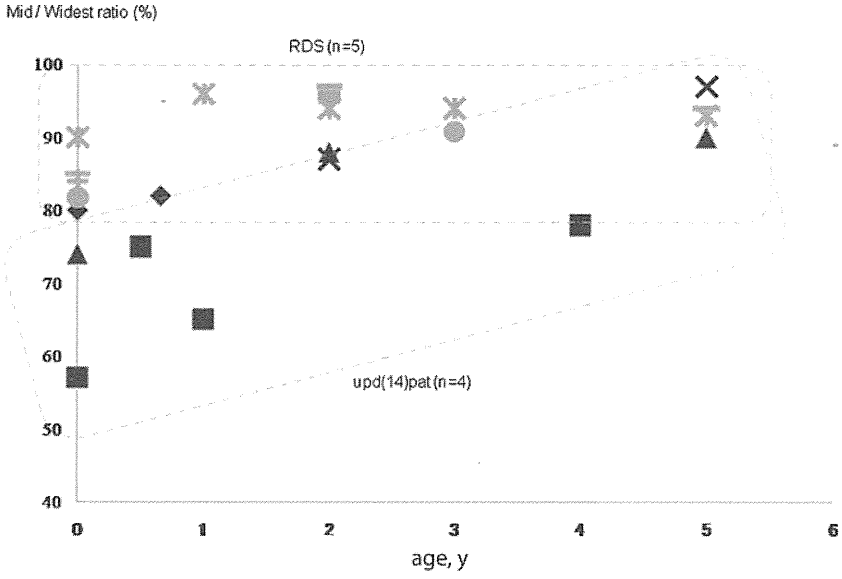

Fig. 6 Comparative observation of age-dependent transition of M/W ratio between the upd(14) pat and RDS groups. Individual shapes represent individual patients

ing thoracic hypoplasia, such as thanatophoric dysplasia, asphyxiating thoracic dysplasia and metatropic dysplasia [13]. However, there are several disorders wherein thoracic hypoplasia is the sole radiological hallmark, including Barnes syndrome, Shwachman-Diamond syndrome and the mildest cases of asphyxiating thoracic hypoplasia. Thus, we thought that quantitative analyses of the coat-hanger sign could elucidate how different the thoracic hypoplasia

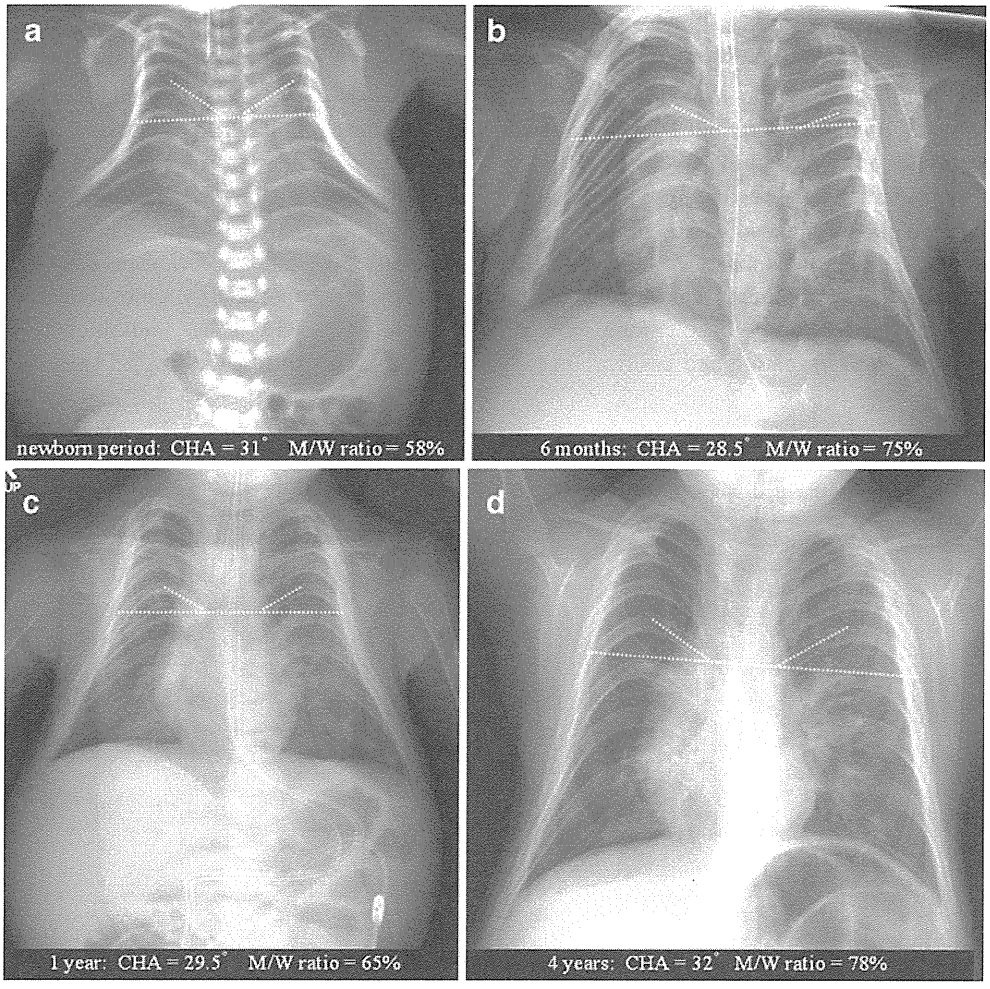

Fig. 7 Serial images of the thorax deformity in upd(14)pat. In this case, four images taken at different ages were available: (**a**) neonatal period, (**b**) 6 months, (**c**) 1 year and (**d**) 4 years. The CHA was almost consistent regardless of age, while the M/W ratio increased with advancing age. The coat-hanger sign and bell-shaped thorax are readily identifiable in the neonatal period. The diagnosis is not straightforward in childhood, yet close observation combined with CHA measurement points to the coat-hanger sign

in upd(14)pat is from the thoracic hypoplasia in other genetic disorders, and presumed that the measurement of CHA (mean 35.1°) and M/W ratio (mean 75.4%) might be helpful when the diagnosis of upd(14)pat is in question. As comparison groups, we included not only cases of severe bone dysplasias but also RDS. Neonates with RDS may present with a small chest [14], and it is not uncommon for them to undergo repeated examinations of chest radiographs because of the association with chronic lung disease.

Kagami et al. [5] reported the age-dependent evolution of the thoracic deformity of upd(14)pat in two children, which was said to ameliorate in mid-childhood. Their observation corresponded with the improvement of the M/W ratio with age described here. By contrast, however, CHA persisted consistently until mid-childhood. This finding indicates that the coat-hanger sign is still discernable during mid-childhood. Radiological findings are presumed to be the only clue to the presence of upd(14)pat after mid-childhood. Serial radiographs (newborn, 2 years and 9 years), as illustrated by Cotter et al. [15] also warrant our observation.

A drawback of this study is that it includes a limited number of cases and available radiographs with uneven quality, such as chest radiographs with some obliquity and radiographs taken in the supine position in the neonatal period vs. the upright position in childhood. Even taking into account these technical problems, however, we believe that our quantitative analyses, particularly the measurement of the CHA, are a valid way to characterize the distinctive thoracic deformity in upd(14)pat.

Conclusion

The coat-hanger sign of upd(14)pat was quantitatively represented by CHA, and was found to be more severe than that seen in other genetic bone diseases and to persist into early childhood; thus, the findings will help in the diagnosis of upd(14)pat even after infancy. By contrast, the bell-shaped thorax represented by M/W ratio was significant only in the neonatal period, and its diagnostic value declined with age.

References

1. Kotzot D (2004) Advanced parental age in maternal uniparental disomy (UPD): implication for the mechanism of formation. Eur J Hum Genet 12:343–346
2. Towner D, Yang SP, Shaffer G (2001) Prenatal ultrasound findings in a fetus with paternal uniparental disomy 14q12-qter. Ultrasound Obstet Gynecol 18:268–271
3. Offiah AC, Cornette L, Hall CM (2003) Paternal uniparental disomy 14: introducing the "coat-hanger" sign. Pediatr Radiol 33:509–512
4. Stevenson DA, Brothman AR, Chen Z et al (2004) Paternal uniparental disomy of chromosome 14: confirmation of a clinically-recognizable phenotype. Am J Med Genet A 130A:88–91
5. Kagami M, Nishimura G, Okuyama T et al (2005) Segmental and full paternal isodisomy for chromosome 14 in three patients: narrowing the critical region and implication for the clinical feature. Am J Med Genet A 138A:127–132
6. Kurosawa K, Sasaki H, Yamanaka M et al (2002) Paternal UPD 14 is responsible for a distinctive malformation complex. Am J Med Genet 110:268–272
7. Yamanaka M, Ishikawa H, Saito K et al (2010) Prenatal findings of paternal uniparental disomy 14: report of four patients. Am J Med Genet 152A:789–791
8. Sutton VR, McAlister WH, Bertin TK et al (2003) Skeletal defect in paternal uniparental disomy for chromosome 14 are re-capitulated in the mouse model (paternal uniparental disomy 12). Hum Genet 113:447–451
9. Mattes J, Whitehead B, Liehr T et al (2007) Paternal uniparental isodisomy for chromosome 14 with mosaicism for a supernumerary marker chromosome 14. Am J Med Genet 143A:2165–2171
10. Irving MD, Bulting K, Kanber D et al (2010) Segmental paternal uniparental disomy (patUPD) of 14q32 with abnormal methylation elicites the characteristic features of complete pat UPD14. Am J Med Genet 152A:1942–1950
11. Georgiades P, Watkins M, Surani MA et al (2000) Parental origin-specific developmental defects in mice with uniparental disomy for chromosome 12. Development 127:4719–4728
12. Kagami M, Sekita Y, Nishimura G et al (2008) Deletions and epimutations affecting the human 14q32.2 imprinted region in individuals with paternal and maternal upd(14)-like phenotypes. Nat Genet 40:237–242
13. Spranger JW (2002) Asphyxiating thoracic dysplasia. In: Spranger JW, Brill PW, Poznanski A (eds) Bone dysplasia, an atlas of genetic disorders of skeletal development, 2nd edn. Oxford University Press, New York, pp 125–129
14. Swischuk LW (2004) Chapter 1. Respiratory system; respiratory distress in the newborn. In: Swischuk LE (ed) Imaging of the newborn, infant, and young child, 5th edn. Lippincott, Williams & Wilkins, Philadelphia, pp 29–36
15. Cotter PD, Kaffe S, McCurdy LD et al (1997) Paternal uniparental disomy for chromosome 14: a case report and review. Am J Med Genet 70:74–79

Biochemical and Biophysical Research Communications 411 (2011) 607–612

Contents lists available at ScienceDirect

Biochemical and Biophysical Research Communications

journal homepage: www.elsevier.com/locate/ybbrc

Induction of chondrogenic cells from dermal fibroblast culture by defined factors does not involve a pluripotent state

Hidetatsu Outani [a,b], Minoru Okada [a,c], Kunihiko Hiramatsu [a,b], Hideki Yoshikawa [b], Noriyuki Tsumaki [a,b,c,d,*]

[a] Department of Bone and Cartilage Biology, Osaka University Graduate School of Medicine, 2-2 Yamadaoka, Suita, Osaka 565-0871, Japan
[b] Department of Orthopaedic Surgery, Osaka University Graduate School of Medicine, 2-2 Yamadaoka, Suita, Osaka 565-0871, Japan
[c] Japan Science and Technology Agency, CREST, Tokyo 102-0075, Japan
[d] Center for iPS Cell Research and Application, Kyoto University, 53 Kawahara-cho, Shogoin, Sakyo-ku, Kyoto 606-8507, Japan

ARTICLE INFO

Article history:
Received 23 June 2011
Available online 6 July 2011

Keywords:
Cartilage
Chondrocytes
Cell reprogramming
Nanog
Pluripotency
iPS cells

ABSTRACT

There is a significant need for cell sources for cartilage regenerative medicine. It has been reported that the combined transduction of two reprogramming factors (c-Myc and Klf4) and one chondrogenic factor (SOX9) directly induces chondrogenic cells from mouse dermal fibroblast (MDF) culture. To gain insights into the process by which cellular characteristics are altered by transduction of c-Myc, Klf4 and SOX9, we examined marker gene expression in the MDF culture at various time points after transduction. The expression of fibroblast-markers was reduced first, followed by an increase in the expression of a chondrocyte-marker. We detected no expression of pluripotent markers at any time point examined. To determine whether or not induced chondrogenic cells go through a pluripotent state after transduction, we analyzed MDFs prepared from Nanog-GFP transgenic mice by monitoring expression of the GFP-labeled pluripotent marker Nanog-GFP in the MDF culture, using time-lapse microscopic observation. Whole-well time-lapse observation revealed that none of the induced chondrogenic cells displayed GFP fluorescence during induction. These results indicate that cells do not undergo a pluripotent state during direct induction of chondrogenic cells from fibroblast culture by transduction of c-Myc, Klf4 and SOX9.

1. Introduction

Articular hyaline cartilage covers the ends of bones and sustains smooth articulation of joints. Hyaline cartilage consists of chondrocytes that are scattered in an extracellular matrix whose properties define the mechanical function of cartilage. Chondrocytes produce cartilage-specific matrix proteins including types II and XI collagens and aggrecan, and thereby assemble cartilage extracellular matrix. Hyaline cartilage has a very weak capacity for repair. Damage of hyaline cartilage due to trauma or degeneration with age is repaired with fibrous scar tissue which is called fibrocartilage [1]. Fibrocartilage contains type I collagen, which is absent in hyaline cartilage and is inferior in mechanical functions to hyaline cartilage. Fibrocartilage is eventually lost due to mechanical stress, resulting in debilitating conditions, such as osteoarthritis. Currently no drugs have been developed that can induce the production of hyaline cartilage. This means that hyaline cartilage needs to be developed using a regenerative medicine approach. Because chondrocytes are limited in number and their expansion in monolayer culture results in dedifferentiation, as indicated by the expression of type I collagen, there is a significant need for cell sources for cartilage regenerative medicine. Induction of chondrogenic cells from dermal fibroblasts using a cell type conversion technique could increase the supply of a cell source for cartilage regenerative medicine. One such approach is to induce pluripotent stem (iPS) cells from dermal fibroblast culture by transduction of c-Myc, Klf4, Oct3/4, and Sox2 followed by redifferentiation into chondrogenic cells. Although this is a promising approach, it is accompanied by a risk of teratoma formation when the cells are implanted *in vivo*, even after redifferentiation into chondrogenic cells, because a trace of residual pluripotent cells can give rise to teratoma [2]. Recently, a second approach has been reported that involves direct induction of hyaline chondrogenic cells from mouse dermal fibroblast (MDF) culture by transduction of two reprogramming factors (c-Myc and Klf4) and the chondrogenic factor Sox9 [3]. Nonchondrogenic cells in MDF culture give rise to the chondrogenic cells, because the number of prechondrogenic cells indicated by Sox9 expression in MDF culture is much lower than the number of chondrogenic colonies which are induced by transduction of

Abbreviations: MDFs, mouse dermal fibroblasts; iPS cells, induced pluripotent stem cells; *Col1a1*, α1(I) collagen chain gene; *Col1a2*, α2(I) collagen chain gene; *Col2a1*, α1(II) collagen chain gene.

* Corresponding author at: Center for iPS Cell Research and Application, Kyoto University, 53 Kawahara-cho, Shogoin, Sakyo-ku, Kyoto 606-8507, Japan. Fax: +81 6 6879 3798.
E-mail address: ntsumaki@cira.kyoto-u.ac.jp (N. Tsumaki).

0006-291X/$ - see front matter © 2011 Elsevier Inc. All rights reserved.
doi:10.1016/j.bbrc.2011.06.194

c-Myc, Klf4, and SOX9 [3]. This technique of direct conversion appears simpler than the approach that involves iPS cells and can therefore shorten the putative reprogramming process. The resulting reduction in excessive reprogramming is likely to contribute to the safety of the induced cells, including reduced genomic aberrations and reduced risk of teratoma formation when implanted *in vivo*. However, it is not clear whether chondrogenic cells induced by this technique that employs c-Myc and Klf4 have, in actuality, not gone through a pluripotent state during the process by which fibroblasts are reprogrammed into chondrogenic cells.

To examine the effects of transduction of c-Myc, Klf4, and SOX9 on the characteristics of MDFs, we analyzed the mRNA expression of pluripotent markers by MDFs over several days after transduction of c-Myc, Klf4 and SOX9 using RT-PCR. Pluripotent markers, including Nanog and Oct3/4, were not expressed. We then analyzed MDFs prepared from Nanog-GFP transgenic mice [4], using real-time monitoring of pluripotent markers. Time-lapse full-scan observation of cells in culture dishes showed that the cells that later became chondrogenic cells exhibited only background levels of Nanog-GFP fluorescence. These results indicate that chondrogenic cells are induced from mouse fibroblast culture without going through a pluripotent state.

2. Materials and methods

2.1. Preparation of Nanog-GFP MDFs

For MDF isolation, skin was prepared from six-week-old Nanog-GFP transgenic mice [4]. After the hair was shaved off, the skin was minced and trypsinized at 37 °C for 4 h. Dissociated cells were filtered through a nylon mesh (pore size, 40 μm; Tokyo Screen, Tokyo, Japan) to generate a single-cell suspension and then seeded onto 100 mm dishes and cultured in DMEM supplemented with 10% FBS (passage 1).

2.2. Retroviral transduction and time-lapse imaging

Retroviral infection was performed as described previously [5]. One day after seeding Plat-E cells [6] at a density of 3.6×10^6 cells per 10 cm dish, we transfected the cells with pMXs-c-Myc (Addgene plasmid 13375), pMXs-Klf4 (Addgene plasmid 13370), pMXs-Oct3/4 (Addgene plasmid 13366), pMXs-Sox2 (Addgene plasmid 13367) [5], and pMXs-hSOX9 by using the Fugene 6 transfection reagent (Roche). Twenty-four hours after transfection, the medium was replaced. Twenty-four hours after medium replacement, the medium was collected as the virus-containing supernatant from Plat-E cultures.

Frozen stored MDFs were thawed, seeded onto 100 mm dishes and cultured in DMEM supplemented with 10% FBS. One day before transduction, the cells were trypsinized and replated at a density of 1.7×10^5 cells per 6 cm dish (passage 3).

The virus-containing supernatants were filtered through a 0.45 μm cellulose acetate filter (Schleicher & Schuell) and were supplemented with 4 μg/ml polybrene (Nacalai Tesque).

Equal amounts of supernatants containing each of the retroviruses (pMXs-c-Myc, pMXs-Klf4, and pMXs-SOX9 for induction of chondrogenic cells; pMXs-c-Myc, pMXs-Klf4, pMXs-Oct3/4, and pMXs-Sox2 for induction of iPS cells) were mixed and added to the MDF cultures (day 0). After overnight (16 h) incubation in the virus-containing medium, the fibroblast culture in the 6 cm dish was trypsinized and replated into six wells of a six-well plate in fresh medium (day 1). The plates were subjected to time-lapse GFP observation using Biostation CT (Nikon). Phase and GFP images were captured every 8 h for 20 consecutive days. Entire wells were each scanned using a total of 64 images (8 rows × 8 columns), and a tiled image was reconstituted. Each image in the movie is shown for 0.5 s, thus 8 h corresponds to 0.5 s. For induction of chondrogenic cells the DMEM medium supplemented with 10% FBS was changed every other day. On day 21, the cells in the dishes were stained with toluidine blue. For induction of iPS cells, the cells were replated on SNL feeder cells at a density of 2×10^4 cells per well in a six-well plate and the medium was changed to ES cell medium the next day according to a previously described method [7].

2.3. Real-time RT-PCR and RT-PCR analyses

RNA was extracted from the MDF cells in culture just before (day 0), and various days after transduction with c-Myc, Klf4, and SOX9 by using RNeasy Mini Kits (Qiagen). Total RNA was digested with DNase to eliminate any contaminating genomic DNA. For real-time quantitative RT-PCR, 1 μg of total RNA was reverse transcribed into first-strand cDNA by using SuperScript III (Invitrogen) and an oligo$(dT)_{20}$ primer. The PCR amplification was performed in a reaction volume of 20 μl containing 2 μl of cDNA, 10 μl of SYBER PremixExTaq (Takara) and 7900HT (Applied Biosystems). The RNA expression levels were normalized to the level of *Gapdh* expression. For RT-PCR analysis, 1 μg of total RNA was reverse transcribed into first-strand cDNA by using SuperScript III (Invitrogen) and oligo$(dT)_{20}$ primers. PCR was performed using the KODFX DNA polymerase (Toyobo). The primers used are listed in Table 1. Control cells that were similarly analyzed were E14tg2a ES cells that were maintained as described previously [8] and the differentiated iPS cells *d-iPS1* and *2* [7].

2.4. Immunohistochemistry

After retroviral transduction of MDFs with c-Myc, Klf4, and Sox9, the cultures were continued for 3 weeks. Following fixation with 4% paraformaldehyde, nodules were picked-up manually, transferred into gelatin, and processed for sectioning for histologic analysis. Immunohistochemical analysis was performed using anti-type II collagen antibody (Thermo #MS-235-P0, dilution

Table 1
Sequences of the PCR primers used.

Primer	Sequence
Col1a1 S	GCAACAGTCGCTTCACCTAC
Col1a1 AS	GTGGGAGGGAACCAGATTG
Col1a2 S	TCGGGCCTGCTGGTGTTCGTG
Col1a2 AS	TGGGCGCGGCTGTATGAGTTCTTC
Col2a1 S	TTGAGACAGCACGACGTGGAG
Col2a1 AS	AGCCAGGTTGCCATCGCCATA
Gapdh S	GAGATGATGACCCTTTTGGCT
Gapdh AS	TCAAGGCCGAGAATGGGAAG
Nanog S	TCTTCCTGGTCCCCACAGTTT
Nanog AS	GCAAGAATAGTTCTCGGGATGAA
Oct3/4 S	CTGAGGGCCAGGCAGGAGCACGAG
Oct3/4 AS	CTGTAGGGAGGGCTTCGGGCACTT
Sox2 S	GGTTACCTCTTCCTCCCACTCCAG
Sox2 AS	TCACATGTGCGACAGGGGCAG
Rex1 S	ACGAGTGGCAGTTTCTTCTTGGGA
Rex1 AS	TATGACTCACTTCCAGGGGGCACT
Utf1 S	GGATGTCCCGGTGACTACGTCTG
Utf1 AS	GGCGGATCTGGTTATCGAAGGGT
Brachyury S	AACTTTCCTCCATGTGCTGAGAC
Brachyury AS	TGACTTCCCAACACAAAAAGCT
Mixl1 S	ACTTTCCAGCTCTTTCAAGAGCC
Mixl1 AS	ATTGTGTACTCCCCAACTTTCCC
Afp S	TGCAGAAACACATCGAGGAGAG
Afp AS	GCTTCACCAGGTTAATGAGAAGC
Sox17 S	TTTGTGTATAAGCCCGAGATGG
Sox17 AS	AAGATTGAGAAAACACGCATGAC

1:200) and anti-Aggrecan antibodies (Santa Cruz, sc-25674, dilution 1:200). Immune complexes were detected using Alexa Fluor 488 (Invitrogen). DNA was stained with Hoechst 33,342 (invitrogen H3570).

All experiments were approved by our institutional animal committee (the Institutional Animal Care and Use Committee (IACUC) of Osaka University Graduate School of Medicine) and institutional biosafety committee (Osaka University Living Modified Organism (LMO) Experiments Safety Committee).

3. Results

3.1. Analysis of fibroblast- and chondrocyte-marker gene expression by MDFs after transduction of c-Myc, Klf4 and SOX9

To gain some insight into the course of the alteration in cell characteristics following transduction of c-Myc, Klf4 and SOX9 into MDFs, we analyzed MDF expression of fibroblast- and chondrocyte-marker genes over several days after transduction, using real-time RT-PCR analysis of MDF RNA (Fig. 1A). The mRNA expression levels of the fibroblast-markers, α1(I) collagen chain gene (*Col1a1*) and α2(I) collagen chain gene (*Col1a2*), were maintained for 1 day after transduction but were reduced 2 days after transduction. On the other hand, the expression level of the chondrocyte-marker gene, α1(II) collagen chain gene (*Col2a1*), was substantially increased on day 5 after transduction. These results suggest that transduction of c-Myc, Klf4 and SOX9 into MDFs decreases fibroblastic characteristics, and this decrease is then followed by acquisition of a chondrogenic phenotype. To confirm that chondrogenic cells were indeed induced in this culture system as previously reported [3], we continued the culture for 3 weeks after transduction and then stained the cells using cartilage-specific stains. Cell aggregates with a nodular appearance were formed in the dishes and displayed metachromatic toluidine blue staining

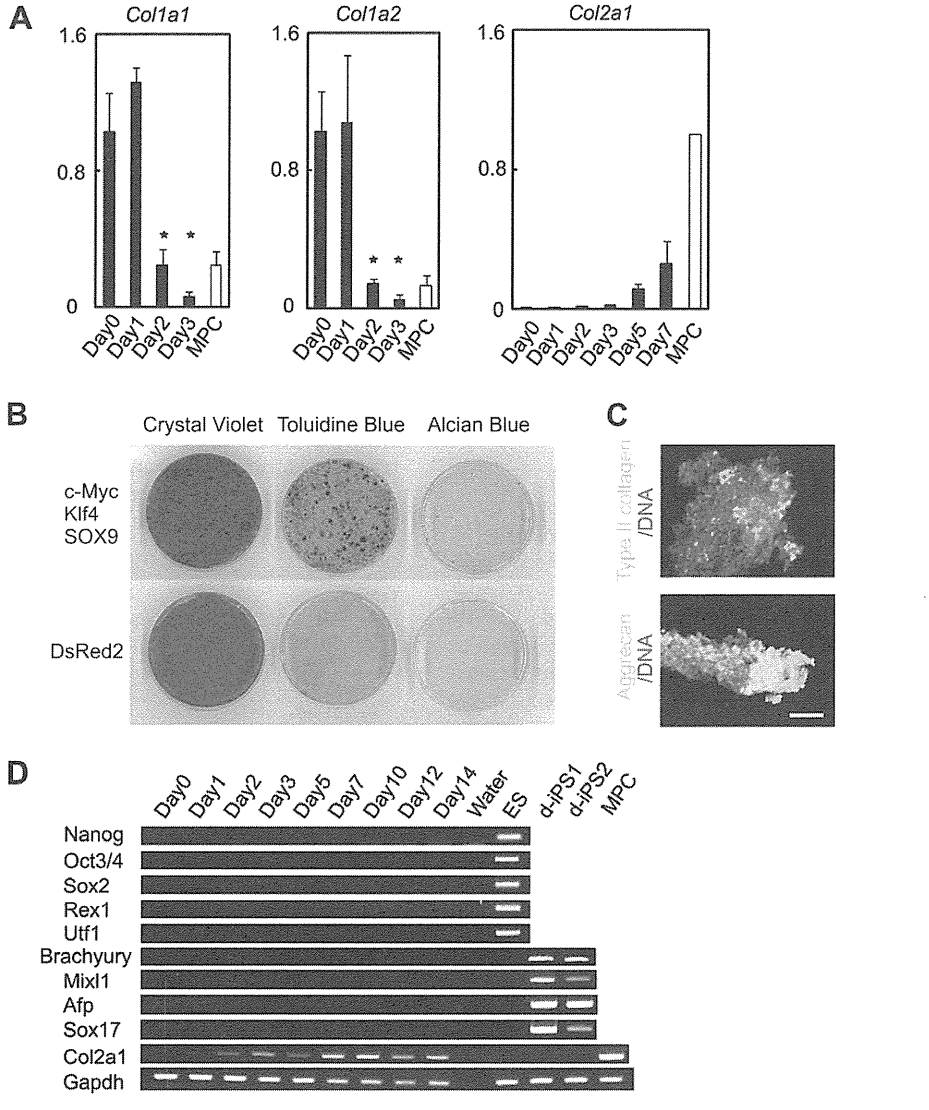

Fig. 1. Analysis of marker gene expression in MDFs after transduction of c-Myc, Klf4 and SOX9. RNA was collected at the time points indicated at the bottom of each graph. (A) Real-time RT-PCR analysis of the mRNA expression of fibroblast- and chondrocyte-marker genes. *MPC*, mouse primary chondrocytes. Error bars indicate mean ± SD ($n = 3$). For *Col1a1* and *Col1a2*, $^{*}p < 0.05$ between samples on day 0 and samples collected at each time point as determined using Student's *t* test. (B) MDF culture dishes stained with crystal violet, toluidine blue or alcian blue 21 days after transduction of c-Myc, Klf4 and SOX9, or DsRed2. (C) Nodules that had formed in the MDF culture dishes 21 days after transduction of c-Myc, Klf4 and SOX9 were picked-up, sectioned and immunostained with anti-type II collagen antibodies (green) and anti-Aggrecan antibodies (green). DNA was stained with Hoechst 33,342 (blue). Scale bar, 100 μm. (D) RT-PCR analysis of the mRNA expression of pluripotent- and developmental-marker genes. *ES*, E14tg2a embryonic stem cells; *d-iPS1* and *2*, differentiated iPS cells; *MPC*, mouse primary chondrocytes.

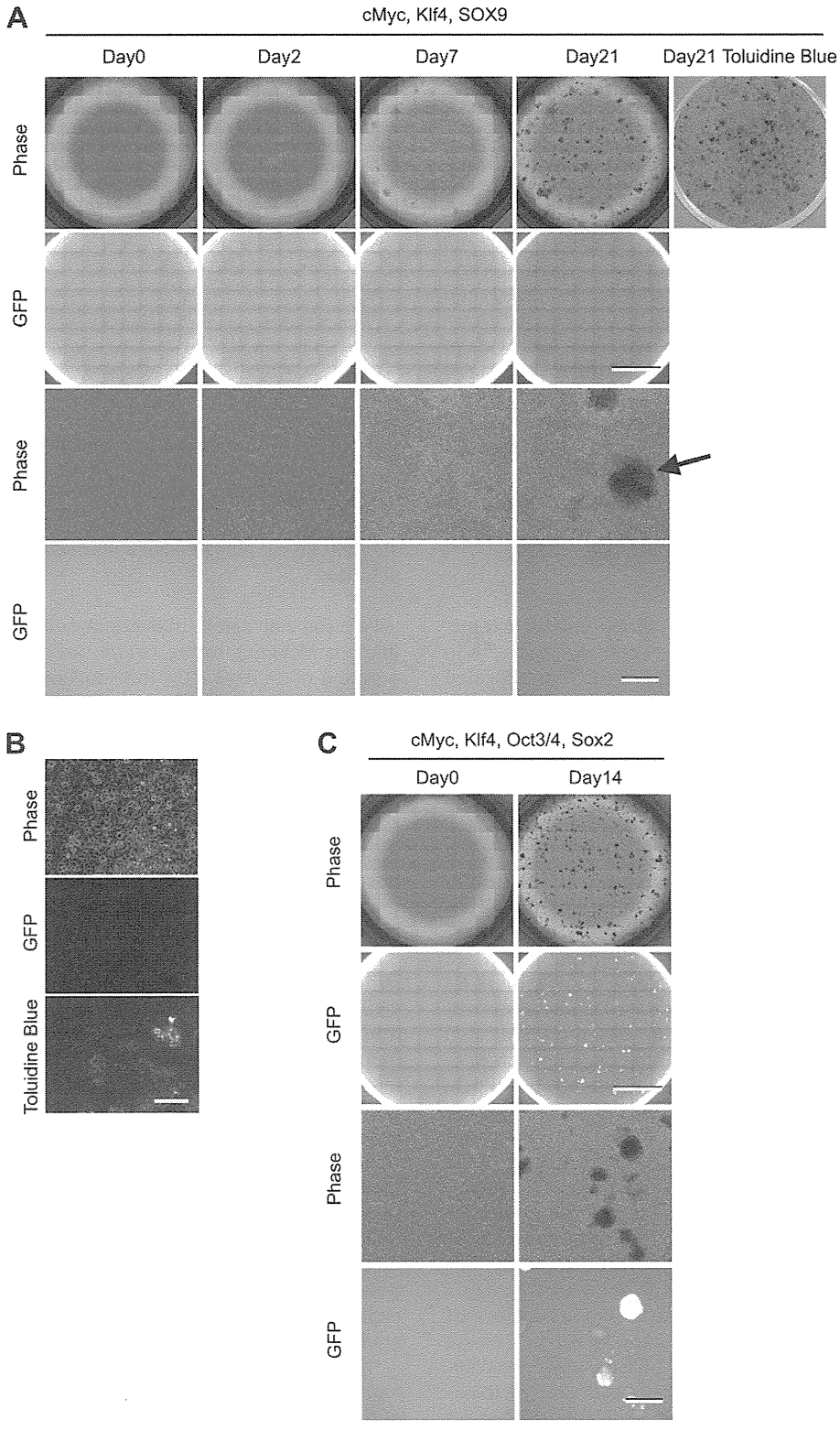

Fig. 2. Time-lapse images of Nanog-GFP MDF culture transduced with c-Myc, Klf4 and SOX9. (A) Time-lapse phase contrast (top row) and GFP fluorescence (second row) tiled images, spanning an entire well of a six-well plate. The top right panel shows toluidine blue staining of the well whose phase image is shown at left. One magnified phase (third row) and GFP fluorescent (bottom row) image is shown. Scale bars: 10 mm in top and second rows; 1 mm in third and bottom rows. (B) Magnification of the nodules indicated by an *arrow* in the right panel in the third row in (A). Scale bar, 100 μm. (C) As a control, Nanog-GFP MDFs were transduced with c-Myc, Klf4, Oct3/4 and Sox2. Phase contrast (top row) and GFP fluorescent (second row) tiled images, spanning an entire well of a six-well plate are shown. One magnified phase contrast (third row) and GFP fluorescent (bottom) image is shown. Scale bars: 10 mm in top and second rows; 1 mm in third and bottom rows (For interpretation of the references to color in this figure legend, the reader is referred to the web version of this article).

and intense Alcian blue staining (Fig. 1B). In addition, immunohistochemical analysis detected type II collagen and Aggrecan immunoreactivity in the nodules (Fig. 1C). These results suggested that chondrogenic cells were induced and formed cartilaginous nodules following transduction.

3.2. Analysis of pluripotent- and developmental-maker gene expression in MDFs after transduction of c-Myc, Klf4 and SOX9

We next examined the expression of pluripotent markers in the MDFs over a period of 14 days after transduction of c-Myc, Klf4 and SOX9, using RT-PCR. Expression of *Nanog*, *Oct3/4*, *Sox2*, *Rex1*, and *Utf1* mRNA were all below the detectable level over the time-course examined, whereas their expression was detected in Embryonic Stem (ES) cells (Fig. 1D). Analysis of the expression of markers of specific developmental stages could not detect expression of genes characteristic of early mesoderm (Brachyury and Mixl1) or of early endoderm (Afp and Sox17) (Fig. 1D). These results suggest that transduction of c-Myc, Klf4 and SOX9 do not guide MDFs to these specific early developmental pathways.

3.3. Time-lapse observation of Nanog-GFP fluorescence during induction of chondrogenic cells

A small number of the cells in the MDF culture that were transduced with c-Myc, Klf4 and SOX9 gave rise to chondrogenic cells in the culture dishes (Fig. 1B) [3]. The majority of the cells appeared as fast-proliferating types of fibroblasts that were transduced with the factors but were not guided to the chondrogenic lineage. To determine whether the induced chondrogenic cells go through a pluripotent stem cell state or not, we monitored pluripotency at the single cell level by using MDFs prepared from Nanog-GFP transgenic mice. Nanog-GFP transgenic mice bear the BAC transgene in which EGFP is inserted into the 5′-untranslated region of the Nanog gene, and express GFP in a pattern that is identical to that of Nanog [4]. To detect potential transient expression of Nanog-GFP, we monitored Nanog-GFP fluorescence at 8 h intervals. An entire well of a six-well plate was analyzed using 64 images (8 rows × 8 columns). To construct a whole-well view, these 64 images were tiled for each well. The time-lapse tiled phase contrast image, which spanned an entire well of a six-well plate, indicated that multiple nodules appeared at 7 days after transduction of c-Myc, Klf4 and SOX9 into Nanog-GFP MDFs (Fig. 2A, top row; Movie S1). These nodules gradually grew in size. Toluidine blue staining showed metachromatic staining of the nodules at 21 days after transduction (Fig. 2A, top right panel), suggesting that these nodule contain glycosaminoglycan and are therefore chondrogenic. Analysis of GFP fluorescence showed background levels of fluorescence throughout the observation period (Fig. 2A, second row; Movie S2). Detailed examination of each image revealed that cells proliferated vigorously on day 2 and started to form nodules by day 7 (Fig. 2A, third row; Movie S3), which is consistent with a previous report [3]. The nodules had become substantial in size by 21 days after transduction (Fig. 2A third right panel). Each nodule was composed of multilayered polygonal-shaped cells and showed metachromatic toluidine blue staining (Fig. 2B), indicating that these cells were chondrogenic. A total of six wells were analyzed in this manner, in which 64 phase contrast and GFP-fluorescent images were captured per well, 3 times a day (8 h intervals), for 20 days. Thus, 23,040 phase contrast and GFP images were captured in total. Nanog-GFP fluorescence was at background levels in all cells, in all 23,040 GFP images, including cells which were later shown to become chondrogenic cells (Table 2; Fig. 2A, bottom; Movie S4). In contrast, the control iPS cells used for this study showed intense GFP fluorescence following transduction of c-Myc, Klf4, Oct3/4 and Sox2 (Fig. 2C; Movies S5–8). Substantial GFP fluorescence was detected as early as 8–9 days after transduction (Movies S6 and S8).

Table 2
Number of nodules showing metachromatic toluidine blue staining and number of cells showing Nanog-GFP fluorescence after transduction of c-Myc, Klf4 and SOX9.

Well of a six-well plate	Number of cells seeded	Number of nodules with metachromatic toluidine blue staining	Number of cells with GFP fluorescence[a]
1	5.1×10^4	20	0
2	5.1×10^4	65	0
3	5.1×10^4	25	0
4	2.5×10^4	12	0
5	2.5×10^4	15	0
6	2.5×10^4	15	0
Total	2.3×10^5	152	0

[a] Sum of numbers of cells showing GFP fluorescence throughout observation.

4. Discussion

4.1. Cells do not pass through a pluripotent state during chondrogenic induction

We did not detect mRNA expression of pluripotent stem cell markers including *Nanog*, *Oct3/4*, *Sox2*, *Rex1*, and *Utf1* in cells over a period of 14 days after transduction of c-Myc, Klf4, and SOX9, using RT-PCR analysis. We also did not detect Nanog-GFP expression above background levels in any of the cultured cells using time-lapse analysis. Based on these results, we concluded that cells do not pass through a pluripotent state during direct induction of chondrogenic cells from fibroblast culture. It has been shown that *in vivo* transplantation of chondrogenic cells that were directly induced from dermal fibroblasts in culture does not result in the production of a teratoma [3]. Our results confirmed that, at least in theory, these induced chondrogenic cells should not produce a teratoma when implanted *in vivo*.

The generation of iPS cells is associated with vigorous epigenetic reprogramming, which can possibly cause DNA damage and genomic instability [9,10]. If the degree of nuclear reorganization during the cell reprogramming process is lower during direct induction of chondrogenic cells from fibroblasts than that during induction through iPS cells, then it is possible that genomic aberrations will also be reduced in the directly induced chondrogenic cells compared with those which are induced through iPS cells.

The sensitivity of detection of GFP fluorescence in our experiment was high, since we were able to detect Nanog-GFP fluorescence during induction of iPS cells as early as day 8–9. We therefore concluded that Nanog-GFP was not expressed by any cell during induction of chondrogenic cells. However, it is still formally possible that we may have missed a very short-lived, transient expression of Nanog-GFP, if the GFP proteins were rapidly degraded in cells during chondrogenic cell induction.

Although efficient induction of iPS cells requires transduction of four reprogramming factors, it has been reported that transduction of three factors (Klf4, Oct3/4, Sox2) can reprogram fibroblasts into iPS cells with low efficiency [11]. Furthermore, transduction of neural stem cells with Oct3/4 alone [12], transduction of certain somatic cells with Oct3/4 in combination with specific chemical molecules [13], or transduction of follicle dermal papilla cells with Oct3/4 alone [14] results in the induction of iPS cells. These findings imply that transduction of fewer reprogramming factors could produce a pluripotent stem cell state, if the appropriate cells or conditions are used. However, the efficiency of iPS cell induction is very low when the number of reprogramming factors is reduced, compared with the 0.1% efficiency of induction of chondrogenic

cells from dermal fibroblast culture [3]. These findings support the notion that cells do not undergo a pluripotent stem cell state during induction of chondrogenic cells from dermal fibroblast culture by transduction of c-Myc, Klf4 and SOX9.

4.2. Sequence of the disappearance of fibroblastic characteristics and chondrogenic commitment

It has been reported that, during induction of iPS cells by forced expression of c-Myc, Klf4, Oct3/4 and Sox2, downregulation of the fibroblast-marker Thy1 occurs first, which is then followed by upregulation of pluripotent markers [15]. Transduction of a combination of c-Myc and Klf4 is the most effective for downregulation of a fibroblast marker, suggesting that c-Myc and Klf4 are responsible for the disappearance of fibroblastic characteristics [16]. In the present study, marked downregulation of *Col1a1* and *Col1a2* mRNA expression began on day 2, and was followed by a gradual upregulation of Col2a1 mRNA expression between days 5–7 after transduction of c-Myc, Klf4, and SOX9. Combined with previous data, it is likely that elimination of the fibroblastic phenotype is induced by c-Myc and Klf4. Commitment and differentiation into chondrogenic cells, which is caused by SOX9, appears to take place once the fibroblast phenotype is eliminated.

In summary, our results indicate that chondrogenic cells induced by c-Myc, Klf4 and SOX9 from MDFs do not pass through a pluripotent state during induction. Such directly induced chondrogenic cells may be safer than chondrogenic cells that were redifferentiated from iPS cells in terms of the risks of teratoma formation and genomic aberrations.

Acknowledgments

We thank Shinya Yamanaka for providing the Nanog-GFP mice and the retroviral vectors. We also thank Toshio Kitamura for the Plat-E cells and the pMX retroviral vectors and Yoshihiro Yoneda for the *d-iPS1* and *2* cells. This study was supported in part by JST, CREST and Scientific Research Grant No. 21390421 from MEXT.

Appendix A. Supplementary data

Supplementary data associated with this article can be found, in the online version, at doi:10.1016/j.bbrc.2011.06.194.

References

[1] A. Bedi, B.T. Feeley, R.J. Williams 3rd, Management of articular cartilage defects of the knee, J. Bone Joint Surg. Am. 92 (2010) 994–1009.
[2] M. Wernig, J.P. Zhao, J. Pruszak, E. Hedlund, D. Fu, F. Soldner, V. Broccoli, M. Constantine-Paton, O. Isacson, R. Jaenisch, Neurons derived from reprogrammed fibroblasts functionally integrate into the fetal brain and improve symptoms of rats with Parkinson's disease, Proc. Natl. Acad. Sci. U S A 105 (2008) 5856–5861.
[3] K. Hiramatsu, S. Sasagawa, H. Outani, K. Nakagawa, H. Yoshikawa, N. Tsumaki, Generation of hyaline cartilaginous tissue from mouse adult dermal fibroblast culture by defined factors, J. Clin. Invest. 121 (2011) 640–657.
[4] K. Okita, T. Ichisaka, S. Yamanaka, Generation of germline-competent induced pluripotent stem cells, Nature 448 (2007) 313–317.
[5] K. Takahashi, S. Yamanaka, Induction of pluripotent stem cells from mouse embryonic and adult fibroblast cultures by defined factors, Cell 126 (2006) 663–676.
[6] S. Morita, T. Kojima, T. Kitamura, Plat-E: an efficient and stable system for transient packaging of retroviruses, Gene Ther. 7 (2000) 1063–1066.
[7] M. Okada, Y. Yoneda, The timing of retroviral silencing correlates with the quality of induced pluripotent stem cell lines, Biochim. Biophys. Acta 1810 (2010) 226–235.
[8] H. Niwa, T. Burdon, I. Chambers, A. Smith, Self-renewal of pluripotent embryonic stem cells is mediated via activation of STAT3, Genes Dev. 12 (1998) 2048–2060.
[9] Y. Mayshar, U. Ben-David, N. Lavon, J.C. Biancotti, B. Yakir, A.T. Clark, K. Plath, W.E. Lowry, N. Benvenisty, Identification and classification of chromosomal aberrations in human induced pluripotent stem cells, Cell Stem Cell 7 (2010) 521–531.
[10] S.M. Hussein, N.N. Batada, S. Vuoristo, R.W. Ching, R. Autio, E. Narva, S. Ng, M. Sourour, R. Hamalainen, C. Olsson, K. Lundin, M. Mikkola, R. Trokovic, M. Peitz, O. Brustle, D.P. Bazett-Jones, K. Alitalo, R. Lahesmaa, A. Nagy, T. Otonkoski, Copy number variation and selection during reprogramming to pluripotency, Nature 471 (2011) 58–62.
[11] M. Nakagawa, M. Koyanagi, K. Tanabe, K. Takahashi, T. Ichisaka, T. Aoi, K. Okita, Y. Mochiduki, N. Takizawa, S. Yamanaka, Generation of induced pluripotent stem cells without Myc from mouse and human fibroblasts, Nat. Biotechnol. 26 (2008) 101–106.
[12] J.B. Kim, V. Sebastiano, G. Wu, M.J. Arauzo-Bravo, P. Sasse, L. Gentile, K. Ko, D. Ruau, M. Ehrich, D. van den Boom, J. Meyer, K. Hubner, C. Bernemann, C. Ortmeier, M. Zenke, B.K. Fleischmann, H. Zaehres, H.R. Scholer, Oct4-induced pluripotency in adult neural stem cells, Cell 136 (2009) 411–419.
[13] S. Zhu, W. Li, H. Zhou, W. Wei, R. Ambasudhan, T. Lin, J. Kim, K. Zhang, S. Ding, Reprogramming of human primary somatic cells by OCT4 and chemical compounds, Cell Stem Cell 7 (2010) 651–655.
[14] S.Y. Tsai, B.A. Bouwman, Y.S. Ang, S.J. Kim, D.F. Lee, I.R. Lemischka, M. Rendl, Single transcription factor reprogramming of hair follicle dermal papilla cells to induced pluripotent stem cells, Stem cells 29 (2011) 964–971.
[15] M. Stadtfeld, N. Maherali, D.T. Breault, K. Hochedlinger, Defining molecular cornerstones during fibroblast to iPS cell reprogramming in mouse, Cell Stem Cell 2 (2008) 230–240.
[16] R. Sridharan, J. Tchieu, M.J. Mason, R. Yachechko, E. Kuoy, S. Horvath, Q. Zhou, K. Plath, Role of the murine reprogramming factors in the induction of pluripotency, Cell 136 (2009) 364–377.

Development 139, 1153-1163 (2012) doi:10.1242/dev.072652

SIK3 is essential for chondrocyte hypertrophy during skeletal development in mice

Satoru Sasagawa[1,3,6], Hiroshi Takemori[4], Tatsuya Uebi[4], Daisuke Ikegami[1,2], Kunihiko Hiramatsu[1,2], Shiro Ikegawa[5], Hideki Yoshikawa[2] and Noriyuki Tsumaki[1,2,3,7,*]

SUMMARY

Chondrocyte hypertrophy is crucial for endochondral ossification, but the mechanism underlying this process is not fully understood. We report that salt-inducible kinase 3 (SIK3) deficiency causes severe inhibition of chondrocyte hypertrophy in mice. SIK3-deficient mice showed dwarfism as they aged, whereas body size was unaffected during embryogenesis. Anatomical and histological analyses revealed marked expansion of the growth plate and articular cartilage regions in the limbs, accumulation of chondrocytes in the sternum, ribs and spine, and impaired skull bone formation in SIK3-deficient mice. The primary phenotype in the skeletal tissue of SIK3-deficient mice was in the humerus at E14.5, where chondrocyte hypertrophy was markedly delayed. Chondrocyte hypertrophy was severely blocked until E18.5, and the proliferative chondrocytes occupied the inside of the humerus. Consistent with impaired chondrocyte hypertrophy in SIK3-deficient mice, native SIK3 expression was detected in the cytoplasm of prehypertrophic and hypertrophic chondrocytes in developing bones in embryos and in the growth plates in postnatal mice. HDAC4, a crucial repressor of chondrocyte hypertrophy, remained in the nuclei in SIK3-deficient chondrocytes, but was localized in the cytoplasm in wild-type hypertrophic chondrocytes. Molecular and cellular analyses demonstrated that SIK3 was required for anchoring HDAC4 in the cytoplasm, thereby releasing MEF2C, a crucial facilitator of chondrocyte hypertrophy, from suppression by HDAC4 in nuclei. Chondrocyte-specific overexpression of SIK3 induced closure of growth plates in adulthood, and the SIK3-deficient cartilage phenotype was rescued by transgenic SIK3 expression in the humerus. These results demonstrate an essential role for SIK3 in facilitating chondrocyte hypertrophy during skeletogenesis and growth plate maintenance.

KEY WORDS: *Col11a2*, HDAC4, SIK3, Chondrocyte hypertrophy, Endochondral bone formation, Knockout mouse

INTRODUCTION

Vertebrate bones develop through membranous or endochondral ossification. Except for craniofacial bones and the clavicle, all bones are established through the latter process (Olsen et al., 2000; Karsenty et al., 2009). At the onset of endochondral bone formation, mesenchymal cells first undergo condensation, followed by differentiation of cells within these condensations into chondrocytes. Chondrocytes then proliferate and produce extracellular matrix to form the primordial cartilage that prefigures the future skeletal elements. Shortly after the formation of the primordial cartilage, proliferating chondrocytes in the central region of the cartilage exit the cell cycle and differentiate into prehypertrophic, and subsequently hypertrophic, chondrocytes. The proliferating chondrocytes closest to the prehypertrophic chondrocytes flatten out and form orderly columns of flat chondrocytes that continue to proliferate. Finally, hypertrophic chondrocytes progress to terminal maturation, following which they express matrix metalloproteinase 13 (MMP13). The terminally matured chondrocytes undergo apoptosis. Blood vessels, along with osteoblasts, osteoclasts and hematopoietic cells, then invade this region and form primary ossification centers. Within these centers, the hypertrophic cartilage matrix is degraded, the hypertrophic chondrocytes die, and bone replaces the disappearing cartilage.

Recent molecular and genetic studies coupled with classical histological approaches have revealed many of the factors that are involved in endochondral bone formation (Lefebvre and Smits, 2005). For example, SOX9 is expressed in mesenchymal progenitor cells and in chondrocytes, but its expression ceases in prehypertrophic chondrocytes (Ng et al., 1997; Zhao et al., 1997). SOX9 has a variety of functions in chondrogenesis: its expression in mesenchymal progenitor cells is essential for cartilage formation (Akiyama et al., 2002); it directly regulates cartilage-specific matrix genes such as the α1(II) collagen chain gene (*Col2a1*), aggrecan (*Acan*) and the α2(XI) collagen chain gene (*Col11a2*); it sustains the survival of proliferative chondrocytes during development (Ikegami et al., 2011); SOX9 overexpression in proliferative chondrocytes suppresses their hypertrophy (Akiyama et al., 2004); and it negatively regulates the transcription of the gene that encodes vascular endothelial growth factor (VEGF), which is expressed by hypertrophic chondrocytes (Hattori et al., 2010).

Regarding the hypertrophic differentiation of chondrocytes, several crucial transcriptional regulators have been identified. Histone deacetylase 4 (HDAC4), a class II HDAC, represses the expression of multiple genes through chromatin remodeling, thereby regulating cell fate. To elucidate the specific role of HDAC4, *Hdac4*-null mice have been generated and were noted to display dwarfism and inappropriate chondrocyte hypertrophy,

[1]Department of Bone and Cartilage Biology, Graduate School of Medicine, Osaka University, 2-2 Yamadaoka, Suita, Osaka 565-0871, Japan. [2]Department of Orthopedic Surgery, Graduate School of Medicine, Osaka University, 2-2 Yamadaoka, Suita, Osaka 565-0871, Japan. [3]Japan Science and Technology Agency, CREST, Tokyo, 102-0075, Japan. [4]Laboratory of Cell Signal and Metabolism, National Institute of Biomedical Innovation, 7-6-9 Asagi, Ibaraki, Osaka 567-0085, Japan. [5]Laboratory of Bone and Joint Diseases, Center for Genomic Medicine, RIKEN, Tokyo 108-8639, Japan. [6]Department of Biology, Osaka Medical Center for Cancer and Cardiovascular Diseases, Osaka 537-0025, Japan. [7]Center for iPS Cell Research and Application, Kyoto-University, 53 Kawahara-cho, Shogoin, Sakyo-ku, Kyoto 606-8507, Japan.

*Author for correspondence (ntsumaki@cira.kyoto-u.ac.jp)

Accepted 5 January 2012